GEOCORONAL STRUCTURE 2, INCLUSION OF A MAGNETIC DIPOLAR PLASMASPHERE

by

James Bishop* and Joseph W. Chamberlain

Department of Space Physics and Astronomy

Rice University, Houston, Texas USA

(NASA-CR-182312) GEOCORONAL STRUCTURE 2, INCLUSION OF A MAGNETIC DIPOLAR PLASMASPHERE (Rice Univ.) 54 p

N88-70145

Unclas
00/92 0114153

*current affiliation: Department of Geophysics and Astronomy, Univ. of British Columbia, Vancouver, Canada

ABSTRACT

Calculations of exospheric quantities (hydrogen atom density, satellite atom fractional density, kinetic temperature, and escape flux) at locations along the Earth-Sun axis in the noon and midnight directions have been extended to incorporate a plasmasphere characterized by a dipolar shape and an empirical temperature profile. This interaction, evaluated with parameter values corresponding to low-to-moderate solar conditions, results in an increased density at outer geocoronal positions; the effect is not dramatic, though, and the resulting exosphere mimics the evaporative case closely, in spite of the control of trajectory parcel content by charge exchange collisions. A careful discussion of the handling of plasmaspheric charge exchange collisions and solar ionization is included, and the effect on the exospheric kinetic distribution is analyzed in terms of pertinent examples. In addition, the geotail is demonstrated to stem primarily from the imposition of an exopause by radiation pressure dynamics.

1. INTRODUCTION

Bishop [1985], hereinafter referred to as GS1, outlined a rigorous formulation for the calculation of exospheric quantities and demonstrated that the action of solar radiation pressure generates an observable geotail and a significant quasi-satellite component of evaporative origin. Earlier studies pointed to the likely explanation of the geotail as a result of radiation pressure perturbation of hydrogen atom motion in the exosphere [Thomas and Bohlin, 1972; Bertaux and Blamont, 1973], but the mechanics involved were not immediately appreciated. The action of radiation pressure on the motion of atoms bound by the planetary gravitational field is primarily to alter angular momentum and may be described in terms of an evolution of the osculating Keplerian orbit. A perturbative study by Chamberlain [1979] along these lines provided a strong hint of an evaporative generation of a "satellite" component by proving that tightly bound atoms eventually crash into the planet. Liouville's theorem (more precisely, the collisionless Boltzmann equation) then requires that these orbits be populated by atoms moving in the reverse sense, so the existence of this component is in no way surprising. The remaining questions thus center on the extent of this satellite component. ("Quasi-satellite" is a more appropriate term, in that atoms moving along bound trajectories have finite flight times. However, the term "satellite" will commonly be used to designate evaporative trajectories that loop the planet, while the Keplerian counterparts will be referred to explicitly.)

In addition to outlining an exospheric formalism, GS1 presented several simple models (evaluated at locations near the Earth-Sun axis) aimed at illuminating the effects of additional mechanisms known to act on the geocorona. An evaporative prototype, constructed by invoking Liouville's theorem along exobase intersecting trajectories, exhibited an extensive

satellite component with an observable geotail and a kinetic temperature profile remarkably similar to that belonging to the corresponding analytic model with a complete satellite component (as defined in Chamberlain [1963]), a reflection of the establishment of a quasi-Maxwellian bound component by radiation pressure dynamics. The inclusion of solar ionization as a simple exponential decay produced no real alteration in the evaporative structure, with a depletion of density at high altitudes being the main effect. Interaction with a simple spherical plasmasphere via resonant charge exchange collisions with thermal protons gave rise to a more dramatic density depletion, corresponding to the conversion of bound component atoms to fast escaping atoms. This interaction also resulted in a considerable erosion of the evaporative satellite atom fractional density, particularly inside the plasmapause, and in increased kinetic temperatures at outer geocoronal locations. The geotail feature was, on the other hand, essentially unaffected by the inclusion of either solar ionization or plasmaspheric charge exchange collisions. The plasmasphere interaction study of GS1 was not intended to be realistic; the plasmasphere model itself was too hot and too dense to mimic the actual terrestrial plasmasphere. However, the results obtained with the simple spherical model are amenable to straightforward interpretation and the central point of GS1 is intended to be general: radiation pressure dynamics determines the trajectory behavior independently of the mechanisms affecting population.

This paper extends the set of studied examples to the inclusion of a somewhat more realistic plasmasphere and a more consistent handling of solar ionization. Taking the pragmatic approach advocated by Chiu et al. [1979] and Li et al. [1983], the revised plasmasphere model incorporates several features that are likely to be significant in modeling the true interaction: the

dipolar shape of the plasmapause, the (O^+, H^+, e^-) polarization electrostatic field, and the variation of plasma temperature along magnetic field lines. Following a brief reformulation of the dynamical framework, the handling of the plasmasphere interaction is considered in detail. Examples of the effect of this interaction on the exospheric kinetic distribution function are then discussed and geocoronal models are presented, in terms of hydrogen atom density, satellite atom fractional density, kinetic temperature, and escape flux. The opportunity is taken to point out and correct a few minor errors present in GS1.

2. DYNAMICAL FRAMEWORK

The fundamental concept in this work is the kinetic distribution function, the evaluation of which allows observable quantities like density, kinetic temperature, and escape flux to be computed. The formalism is based on simple Hamiltonian mechanics and is developed along the lines of the analytic theory of Chamberlain [1963]. This allows for straightforward, insightful interpretation of exospheric features and provides a framework for the inclusion of increasingly complicated "corrections"; in particular, it can incorporate realistic exobase and plasmasphere models and is not limited to the simple cases studied here. The current choices are motivated by a belief that an interpretative background must be established prior to attempts at extensive modeling.

In this paper and in the accompanying paper on geocoronal line profiles [Bishop and Chamberlain, 1986], the points of evaluation have been chosen to lie exactly on the Earth-Sun axis. This reduces the dynamical complexity of the motion to two dimensions (neglecting the solar motion across the sky). In terms of the dimensionless quantities of GS1, the appropriate trajectory

equations are

$$\frac{d\lambda}{d\tau} = -\lambda^2 \psi \cos\delta$$

$$\frac{d\chi}{d\tau} = \lambda \psi \sin\delta$$

$$\frac{d\psi}{d\tau} = \frac{-\lambda^2 \cos\delta}{2} - \alpha \cos(\delta + \chi) \qquad (1)$$

$$\frac{d\delta}{d\tau} = \frac{\lambda}{\psi} \sin\delta \left(\frac{\lambda}{2} - \psi^2\right) + \frac{\alpha}{\psi} \sin(\delta + \chi)$$

where δ, the momentum zenith angle, is retained for ease in following reversals of the orbital sense. These equations, when propagated into the past and future from a specified phase point (i.e., the initial position and momentum) determine the exobase and/or exopause intersections. An exobase intersection guarantees the trajectory is populated according to Liouville's theorem for motion in the reverse sense; exopause intersection signifies escape from the planet. (As defined in GS1, the exopause is the radial shell beyond which the radiation pressure induced acceleration exceeds the planetary gravitational acceleration.) Evaluation of the Boltzmann collision integral step by step along the flight path is the method used to incorporate the plasmasphere interaction. Often in the discussion, reference will be made to "trajectory parcels." A parcel of this sort represents a group of atoms occupying a small volume $\underline{dr}$ about a specified location $\underline{r}$, all of which have velocities in the neighborhood $\underline{dv}$ about a velocity $\underline{v}$, in effect sharing a common trajectory. It is synonymous with the kinetic distribution. The interaction with the plasmasphere via resonant charge exchange collisions amounts to the gain or loss of atoms from such a parcel.

In carrying out the computations at locations on the Earth-Sun axis, an

offset of 2° is introduced to the axis along which the GS1 calculations were performed. The evaporative models (classical exobase, solar radiation pressure acting) of this paper and GS1 are, however, identical in all respects. The restriction to axial or near axial locations is mostly a matter of computational expense, in that those trajectories that do not (nearly) intersect the Earth-Sun axis can exhibit fairly complicated behavior. Also, it is simpler to incorporate a dipolar plasmasphere in the calculations when the points of evaluation lie in the magnetic equator. Note that the inclusion of a dipolar plasmasphere lifts the axial symmetry present in the examples discussed in GS1. Thus in the evaluation of a quantity like density, the integral over steering angle (ε) orientations (refer to GS1 Figure 1) cannot be reduced to a factor of 2π but must be explicitly evaluated. Taking the Earth-Sun axis to lie in the magnetic equator, the ε-integral is conveniently handled by rotating the plane of motion (also called the dynamical plane) with respect to the magnetic equatorial plane about this axis. A remaining symmetry permits this integral to be evaluated as

$$\int_0^{2\pi} d\varepsilon \rightarrow 4 \int_0^{\pi/2} d\varepsilon$$

To emphasize the fundamental role of radiation pressure dynamics in determining the structure of an exosphere, consider the occupied or populated volume of velocity space Δ_V at a particular location

$$\Delta_V = 2\pi \iint_{BOUND} \psi^2 \, d\mu \, d\psi, \quad \mu = \cos\delta \tag{2}$$

where the bound component alone is considered since this dominates the density out to great distances, and consider the ratio of volumes along the midnight

($\chi = 180°$) axis to those along the noon ($\chi = 0°$) axis. Figure 1 compares the evaporative geotail ratio and this ratio of occupied volumes. It is evident that the former is a manifestation of the latter. This relative enhancement of bound component volume in the velocity space along the midnight axis derives from the variation of the minimum escape speed with location and direction of motion (refer to GS1, Figure 2 for an illustration). It corresponds to an average minimum escape speed being greater at midnight axis locations than at equi-radial positions along the noon axis, an average that is biased toward trajectories with non-zero transverse velocity components by a factor sin δ. Note that these barely escaping trajectories would simply be high apogee Keplerian ballistic orbits in the absence of radiation pressure. Such an orbit threading the noon axis can be converted by the action of radiation pressure into an escaping trajectory during the segment of flight where $\underline{v} \cdot \underline{a} > 0$ after "apogee" ($\underline{v}$, $\underline{a}$ denote the instantaneous velocity and the radiation pressure acceleration, respectively). For a similar trajectory threading the midnight axis, however, such an "apogee" indicates the trajectory then heads toward the sun ($\underline{v} \cdot \underline{a} < 0$), requiring a greater local velocity to either eliminate such a turning point altogether or at least to remain well out from the planet long enough to undergo a substantial enough shift in angular momentum to attain $\underline{v} \cdot \underline{a} > 0$). In brief, the geotail stems primarily from the imposition of an exopause by radiation pressure dynamics. The difference between the two curves of Figure 1 reflects the dependence of the geotail on population mechanisms, conveyed by the Boltzmann factor of the exobase kinetic distribution in the simple evaporative case, i.e., a smaller exobase speed is required to ascend to great heights on the nightside of the planet.

3. PLASMASPHERE INTERACTION

The Boltzmann Equation

The Boltzmann equation, as used in these calculations, is

$$\frac{df_n(r,p_i')}{dt} = \iiint d^3p_j' \; Q(g)g[f^*(r,p_i')f_n(r,p_j') - f^*(r,p_j')f_n(r,p_i')] \tag{3}$$

collapsing spatial variables to r and momentum variables to p' in the arguments, where Q(g) is the cross section for resonant charge exchange, g is the relative collision speed, and the primed momenta denote the vectorial counterparts to the canonical momenta. (This association is unambiguous in spherical coordinates.) The assumption of no momentum transfer has been applied: the particles involved in the collision simply switch identities. The derivative on the left-hand side denotes the evolution of the neutral kinetic distribution $f_n(r,p_i')$ following the trajectory defined by the local position and momentum.

Writing $f_n = f_o(1 + \Phi)$, where f_o is the evaporative solution (i.e., $df_o/dt = 0$) and $(1 + \Phi)$ is the plasmasphere enhancement factor, Eqn. (3) becomes

$$\frac{d\Phi(i)}{dt} = \frac{Q}{f_o(i)} \; [f^*(i) \iiint g \, f_n(j) d^3p_j' - f_n(i) \iiint g \, f^*(j) d^3p_j'] \tag{4}$$

further collapsing the arguments to the momentum index. As in GS1, Q(g) has been set to a constant value of 4.5×10^{-15} cm^2. The proton kinetic distribution f^* in this work is taken to be Maxwellian in form:

$$f^* = \frac{N^* e^{-\psi^2/\rho^*}}{(2\pi m k T_c \rho^*)^{3/2}}, \quad \rho^* = T^*/T_c \tag{5}$$

The plasmaspheric proton density N^* and temperature $\rho^* T_c$ are derived from simple models described below. Collisions involving O and O^+ are ignored. The idealization of a classical exobase has been retained, which is admittedly unrealistic [Fahr and Shizgal, 1983]. It is worthwhile to point out, though, that the approach taken here can be extended to treat the transition zone in a more satisfying manner and that, as discussed below, H, H^+ collisions alone go a long way toward lifting the idea of a sharp exobase.

Within the above-stated assumptions, the destruction term can be rigorously evaluated:

$$\iiint g f^*(r, p_j') \, d^3 p_j' = N^* g^*$$

$$g^* = \frac{U^*}{\pi^{1/2}} \left[e^{-\psi^2/\rho^*} + \rho^{*1/2} J(\psi/\rho^{*1/2}) \left(\frac{2\psi}{\rho^*} + \frac{1}{\psi} \right) \right] \tag{6}$$

where $U^* = \rho^{*1/2} U_c$ is the most probable proton speed and $J(y) = \int_0^y \exp(-x^2) dx$. ($U_c$ is the most probable hydrogen atom speed at the exobase: $U_c = \left(\frac{2kT_c}{m}\right)^{1/2}$.) In GS1, an incorrect approximation was applied. The effective collision speed g^* was there taken to have the form $U^* \rho^{*1/2} \left(\frac{\psi}{\rho^*} + \frac{1}{2\psi} \right)$, which is plausible only when $\psi > \rho^{*1/2}$. Since almost all neutral atoms are encompassed by the velocity range $0 < \psi < \rho^{*1/2}$, the exact result of Eqn. (6) has been used here.

To handle the creation term, a quasi-iterative approach has been relied upon and an analytic exosphere sharing the prescribed exobase parameters has been used as a zeroth-order approximation. In GS1, the selection of $r_{cs} = 2.50\ R_E$ was motivated by model reductions of outer geocoronal Lyman-α in-

tensity measurements carried out on OGO 5 and Mariner 2 [Bertaux and Blamont, 1973; Wallace et al., 1970]. To explore the effect on the calculations of varying the prescribed r_{cs} value in the creation term, analytic exospheres with $r_{cs} = r_c$ and $r_{cs} = r_p$ have been considered. These two cases must bracket the true situation as regards the interplay between the quasi-satellite component and the plasmasphere. The neutral atoms entering into the creation collisions are imagined to exemplify an isotropic Maxwellian kinetic distribution. This is a convenient picture which is allowable in that momentum transfer has already been neglected and the ions are not followed explicitly; it is also consonant with the action of radiation pressure. The local neutral density in the collision integral is accordingly approximated by an analytic model with an isotropic Boltzmann factor characterized by the effective kinetic temperature appropriate to this model:

$$\iiint g f_n(r, p_j') d^3 p_j' = N_n g_n$$

$$g_n = \frac{U_n}{\pi^{1/2}} \left[e^{-\psi^2/\rho_n} + \rho_n^{1/2} J(\psi/\rho_n^{1/2}) \left(\frac{2\psi}{\rho_n} + \frac{1}{\psi} \right) \right] \tag{7}$$

where $U_n = \rho_n^{1/2} U_c$ and

$$N_n = N_c e^{-(\lambda_c - \lambda)} \Xi(\lambda)$$

$$\rho_n = \frac{2}{3} \left[\langle \psi^2 \rangle - \xi_{effusion}^2 \right] \tag{8}$$

(see Chamberlain, 1963, Eqns. (15) and (49)-(51) with $\psi^2 \to \psi$ and $\Xi \to \zeta$). This corrects a minor oversight in GS1, wherein the neutral component in the creation integral was treated as if it maintained a kinetic temperature T_c

throughout the plasmasphere.

Another revision of the approach in GS1 is to retain the α-potential in the expression for f_o -

$$f_o = \frac{N_c\, e^{-(\lambda_c - \lambda)}\, e^{-\psi^2}}{(2\pi m k T_c)^{3/2}} \exp\left[-2\alpha\left(\frac{\cos(\chi(\lambda))}{\lambda} - \frac{\cos(x(\lambda_c))}{\lambda_c}\right)\right] \qquad (9)$$

While this factor is not considered significant within the plasmasphere, keeping it does not impose additional hardship.

Collecting and normalizing the time element,

$$\frac{d\Phi(r,p_i')}{d\tau} = P - L \qquad (10)$$

$$P = \frac{QN^*}{(U_c^3/2GM)}\, e^{(\rho^*-1)\psi^2/\rho^*}\, g_n\, \Xi(\lambda) \exp\left[+2\alpha\left(\frac{\cos\chi}{\lambda} - \frac{\cos\chi_c}{\lambda_c}\right)\right]$$

$$L = \frac{QN^*}{(U_c^3/2GM)}\, g^* \left(1 + \Phi(r,p_i')\right)$$

where $\Xi(\lambda)$ is calculated according to the chosen zeroth-order analytic model and g_n is evaluated with the corresponding kinetic temperature. This expression can now be integrated along a trajectory to determine the net accumulation arising from the plasmasphere interaction. (Initial values for Φ are straightforward: for trajectories launching from the exobase $\Phi(\lambda_c) = 0$, while along capture trajectories (i.e., reversed escape trajectories) $\Phi(\lambda_{pp}) = -1$ is appropriate.)

Plasmasphere Models

Two models of the H^+ population have been utilized in this study. Table 1 displays the pertinent parameters and assumed values for each. The

spherical isothermal model of GS1, while unrealistic, has been used because it permits a clear insight into the effect of charge exchange collisions on trajectory parcels and thus into how this affects observable exospheric quantities. It is characterized by a uniform exobase density N_c^*, a constant temperature T^*, and a plasmapause radius r_{pp} ($f^* = 0$ for $r > r_{pp}$); also, diffusive equilibrium is assumed:

$$N^* = N_c^* \, e^{-(\lambda_c - \lambda)/\rho^*}$$

Retaining the GS1 parameter values permits a direct comparison with the earlier results.

The dipolar model is characterized by a dipolar plasmapause of specified L-value L_{pp} and is filled with an (O^+, H^+, e^-) plasma in diffusive equilibrium; the topside ionospheric densities and temperatures of these species are taken to be independent of latitude and local time. The proton density is obtained by using the fluid momentum equation incorporating gravitational and polarization electrostatic fields and the relation $P^* = N^* k T^*$ for the proton pressure P^* (reflecting the assumption of a collisional plasma), and by assuming zero net flow and magnetic field guidance of diffusion. Even though this last assumption is not quite consistent with the idea of a collision-dominated plasma, it yields results reminiscent of observed density profiles [Chiu et al., 1979; Li et al., 1983]. The plasma temperature in this treatment is given by an analytic model to avoid having to consider an energy balance equation [Chiu et al., 1979]:

$$T^* = T_o + \Delta T \left(\frac{L - L_c}{L_o}\right)^{\beta} \left(\frac{s}{\ell}\right)^{\gamma} \qquad (11)$$

where s is the arclength along the field line specified by L from the exobase to the local point and ℓ is the arclength extending to the magnetic equator. In this expression, T_o denotes the plasma temperature at the exobase, ΔT the increase in plasma temperature between the exobase and the hotter outer plasmasphere, L_c the equatorial L-value for the exobase, and L_o a reference magnetic field line roughly indicating where the outer plasmasphere temperature is attained, while β, γ are profile shape parameters. For species i, the resulting density profile is, for $L < L_{pp}$,

$$N_i^*(s) = N_i^*(0) \left[\frac{B(s)\, T^*(0)}{B(0)\, T^*(s)}\right] \exp\left[\int_0^s \left(\frac{mF_i(s')}{kT^*(s')}\right) ds'\right] \tag{12}$$

where B is the dipolar magnetic field strength and the composition has been specified at the exobase. The integration is along the appropriate magnetic field line ($\hat{s}$ ascends from the exobase). The force component F_i along the field direction is the sum of gravity and electrostatic forces. Resolving these and expressing the field line integral in terms of magnetic latitude Λ,

$$\int_0^s \frac{mF_i}{kT^*}\, ds' = G_i + \phi_i$$

$$G_i = -2GMm_i \frac{\cos^2\Lambda_c}{r_c} \int_\Lambda^{\Lambda_c} \frac{\sin\Lambda'}{kT^*(\Lambda')\cos^3\Lambda'}\, d\Lambda' \tag{13}$$

$$\phi_i = \frac{1}{2}\, \ell n \left[\frac{N_e(0)\exp(G_e)}{\sum_{\text{ions}} N_i(0)\exp(G_i)}\right]$$

where the electrostatic potential term is fixed by assuming charge neutrality and zero net flow. The parameter values selected in the calculations correspond roughly to magnetically quiet periods in conjunction with low-to-moderate solar activity conditions (refer to Table 1).

Inclusion of Solar Ionization

Solar ionization processes (photoionization and charge exchange collisions with solar wind protons) can be easily incorporated within the current formalism by looking upon these as a simple exponential decay with dimensionless decay time τ_S. Writing

$$f_n(\tau) = f_o e^{-\tau/\tau_S} + \int_0^\tau d\tau' \; e^{-(\tau-\tau')/\tau_S} \; f_o\left(P(\tau') - L(\tau')\right) \qquad (14)$$

for the kinetic distribution along a trajectory, where P and L represent the plasmaspheric production and loss terms in Eqn. (10), and assuming L to be in the form $q(\tau)f(\tau)$, where q contains the plasmasphere and cross section information, then

$$e^{\tau'/\tau_S}\,(P-L) = e^{+\tau'/\tau_S}\,P(\tau') - q(\tau')\left[f_o + \int_0^{\tau'} d\tau''\; e^{+\tau''/\tau_S}\; f_o\left(P(\tau'')-L(\tau'')\right)\right]$$

The numerical scheme used in this work computes (P - L) for a discrete time interval $\Delta\tau$ in terms of the kinetic distribution accumulated over previous steps. The formulation is then consistent and the production term as expressed above alone acquires the $\exp(+\tau/\tau_S)$ factor - i.e., in terms of the enhancement factor

$$(1+\Phi) = e^{-\tau/\tau_S}\left[1 + \int_0^\tau d\tau'\left(e^{+\tau'/\tau_S}\; P(\tau') - L(\tau')\right)\right] \qquad (15)$$

The value of the decay time $\tau_S = (U_c^3/2GM)T_{sol}$ chosen is biased towards photoionization as the main ionization loss mechanism (refer to Table 1). This inclusion of solar ionization into the Boltzmann collision integral considerably extends the flexibility of the GS1 formalism.

Examples of the Neutral Kinetic Distribution Function

Figure 2 presents two examples of a kinetic distribution evaluation, corresponding to interaction with the spherical (curve S) and the dipolar (curve D) plasmasphere models. The generation of a capture component (downward moving atoms with escaping speeds) and the enhancement of the outward moving escape component are both evident near 2.00 R_E. Interaction with the spherical plasmasphere model shows these effects clearly; the cooler, less dense dipolar plasmasphere model is not as effective in generating a recognizable nonthermal component. The effect on the corresponding bound components is highlighted in Figure 3, by plotting $(1 + \phi)$ on a linear scale. The dipolar plasmasphere model leads to an increase in the bound kinetic distribution at these altitudes and higher, due to charge exchange generation of higher speed neutrals by the 2000K protons near the exobase; use of the warmer spherical plasmasphere model decreases the bound kinetic distribution in the manner discussed in GS1. In either case, though, the modification is not large due to the limited exposure to the plasmasphere of the trajectory parcels represented in this figure (vertical motion).

Figure 4 shows $(1 + \phi)$ for horizontal motion ($\mu = 0$) for bound component speeds at two Earth radii. The maximum isotropic speed ψ^1 acts as a lower limit of satellite speeds, in that for $\psi < \psi^1$ all trajectories directly arise from and return to the exobase without intervening loops. Parcels on trajectories with $\psi > \psi^1$ have a much longer exposure to the plasmasphere, with much more noticeable effect. (Note that this ψ^1 discontinuity arises naturally with the assumption of an ideal exobase.) In this case, the spherical plasmasphere model causes considerable depletion, mitigated somewhat at higher

speeds. Interaction with the dipolar plasmasphere model produces an enhancement at speeds slightly greater than ψ^1 that is striking; these speeds correspond to trajectories having near-exobase perigees. The results obtained using the dipolar plasmasphere model are here shown for two orientations of the plane of particle motion with respect to the magnetic equator. Although the 90° orientation example includes orbits passing over the polar regions where no charge exchange collisions occur, there is not much difference between it and the 0° curve representing motion in the magnetic equatorial plane.

The kinetic distributions evaluated in this paper exhibit smoother behavior with respect to ψ than in the GS1 treatment of the plasmasphere interaction. In particular, referring to GS1 Figure 3, the strong depletion after apogee of kinetic parcels on trajectories having insufficient energy to pierce the plasmapause (segment B in that figure, which also exhibits a computational discontinuity at $\psi = 0$) is due to the inappropriate expression used for the effective collision speed in that paper, as discussed earlier; namely, the $1/\psi$ term becomes large near apogee, when this is within the plasmasphere, leading to a large overestimate of the loss term. Although the bound component response in the GS1 treatment was thus exaggerated, it is still expected that trajectories rising above the plasmapause ought not to be as strongly depleted as those remaining entirely within a hot plasmasphere, and this behavior is clearly shown in Figure 3 in conjunction with the spherical plasmasphere model by the pronounced minimum near $\psi = 1.6$ ($\mu = -1$).

The effect of solar ionization (SI) mechanisms, incorporated via Eqn. (15), is also shown in Figures 3 and 4 in conjunction with the dipolar plasmasphere model (averaged over plane of motion orientation with respect to the magnetic equator). Those trajectory parcels with longer flight times

(downward moving atoms with high apogees in Figure 3, looping atoms in Figure 4) are affected considerably. These figures also illustrate the relative insensitivity of the charge exchange collision integral evaluation to the selection of the r_{cs} parameter in the analytic models used in the creation term, demonstrated here in conjunction with the spherical plasmasphere model. The larger values of Ξ for $r_{cs} = r_p$ increase the net value of $(1 + \phi)$, since this enters into the computations as a multiplicative factor. The variation is small, though, since Ξ itself exhibits small variation throughout that region of the plasmasphere where most of the charge exchange collisions occur. The variation of the results with r_{cs} in conjunction with the dipolar plasmasphere model is even smaller, since most collisions then occur closer to the exobase.

To further illustrate the kinetic modifications arising in the plasmasphere interaction, the $(1 + \phi)$-evolution is shown along several selected trajectories in Figures 5-9. The net accumulation as a function of fractional flight time along a ballistic trajectory that remains within both plasmasphere models (vertical motion, apogee at 3.65 R_E) is shown in Figure 5. The enhancement factor is remarkably unchanging and close to unity with the dipolar plasmasphere model while the spherical plasmasphere model results in the familiar depletion, with slight enhancements ($d\phi/dt > 0$) occurring near the exobase where the highest speeds are attained. The smooth behavior of the $(1 + \phi)$ variation might be noted. Figure 6 illustrates the net accumulation along an escaping trajectory as a function of flight time between the exobase and geosynchronous radius for both ascending and descending motions, most of which is gained below 2.00 R_E. The greater enhancement with the spherical plasmasphere model complements the ballistic parcel erosion illustrated in Figure 5. This is not a particularly fast trajectory, showing only moderate

enhancement.

Figure 7 shows the variation of $(1 + \Phi)$ over an orbit of a trajectory that loops the planet many times, for three orbits. The earliest orbit, with a perigee still close to the exobase, exhibits portions where $d\Phi/dt > 0$ even for interaction with the spherical plasmasphere model; these occur near perigee where the speed is largest. By orbit 15, the motion has circularized to some extent, so that the variations are milder, while in the last orbit shown (orbit 27) perigee is again approaching the exobase, with $\frac{d\Phi}{dt} > 0$ contributions becoming more evident. Again, two orientations are shown for motion through the dipolar plasmasphere, with the 90° orientation of the plane of motion resulting in a weaker interaction. Since the dipolar plasmasphere introduces regions over the magnetic poles devoid of dense plasma, tightly bound trajectories not lying in the magnetic equator can possess plasmapause passages and so have segments of flight where $\frac{d\Phi}{d\tau} = 0$. Such segments occur along the D, 90° trajectory of Figure 7, though these are not easily discerned because of the apparent balance in the interaction with this plasmasphere model. As an aside, this trajectory is a good example of a tightly bound trajectory to which the development of Chamberlain [1979] is applicable - namely, this trajectory exhibits many loops around the planet with small changes in orbital parameters per loop.

The evolution of $\frac{1}{(1+\Phi)} \frac{d\Phi}{d\tau}$ along the trajectory orbits of Figure 7 for two cases is shown in Figure 8, in terms of the separate creation and loss terms of Eqn. (10). Since the speed of an exospheric trajectory is fastest near perigee (and is particularly fast for orbiters near the exobase), the relative magnitude variations of the production terms along this trajectory grow near perigee with both plasmasphere models and indicate a rapid content buildup of trajectory parcels near the exobase. It is also evident that away from the

exobase, loss terms dominate. Away from the exobase, both slower trajectory speeds and higher plasma temperatures guarantee that collisions preferentially result in loss from bound trajectory parcels by conversion to faster moving atoms. Indeed, near 2.00 R_E the most probable proton speeds for both plasmasphere models are greater than the local escape speed. With the dipolar plasmasphere model, though, the loss term is negligible compared to that evaluated with the spherical plasmasphere model because of the smaller H^+ densities, which derive from the fall-off with magnetic intensity coupled with smaller scale heights. The loss terms vary in phase with the production terms, reflecting the proportionality of these terms to N^*.

Figure 9 is meant to illustrate the evolution of $(1 + \Phi)$ over the entire looping flight of the trajectory of Figure 7, by showing the value of $(1 + \Phi)$ at the evening terminator for each orbit (taken to represent an orbit-averaged value). For the first few orbits, the creation term dominates during segments of flight near perigee, offsetting the depletion occurring elsewhere to some extent and keeping $(1 + \Phi)$ near unity. As the orbit circularizes, the $d\Phi/dt > 0$ contributions decrease, and the average value decreases from one orbit to the next. Eventually perigee again moves close to the exobase, so that average values can rise. The 90° orientation of motion through the dipolar plasmasphere shows again a milder variation as the orbit evolves, due to the portions of flight outside the plasmasphere over the polar regions. The dipolar plasmasphere model overall, due to the cooler plasma temperatures near the exobase, results in a net enhancement to the satellite trajectory parcels in this example.

The magnitude of variation shown in Figures 5-9 demonstrates the plasmasphere interaction control of trajectory parcel contents. The fact that both the production and loss terms can exhibit relative magnitude variations on the

order of unity for certain segments of flight indicates that the atoms contained in a trajectory parcel at launch from the exobase are efficiently displaced by charge exchanged atoms, particularly if the parcel belongs to a trajectory that loops the planet several times with near-exobase perigees. In view of this, it is somewhat remarkable that the kinetic distribution obtained using dipolar plasmasphere model resembles the evaporative case so closely. Indeed, the apparently "weak" interaction with the dipolar plasmasphere model shown in Figures 5 and 7 actually conceals a near balance between the production and loss terms of Eqn. (10). At higher speeds, as in Figure 6, the kinetic activity is unveiled. Likewise, trajectory parcels with slow launch speeds (and so unable to climb to 2.00 R_E) suffer a net loss of atoms. With such speeds, however, the relative depletion are not large because of the brief flight times involved. An indication of this is provided in Figures 3 and 4, where the enhancement factors $(1+\Phi)$ evaluated at 2.00 R_E with the dipolar plasmasphere model are less than unity for $\psi < \psi^1$, but not by much. When the interaction is evaluated with the spherical plasmasphere model, the loss term is not matched by gain until higher speeds are considered ($\psi \approx \psi_{ESC}$ for the parameter values selected here). It might also be noted that the inclusion of H, H^+ collisions erases to some extent the initial idealization of an exobase: the exchanges $H \rightleftarrows H^+$ proceed so rapidly near 500 km altitude that any errors introduced by the assumption

$$f_C \propto \frac{N_C e^{-\psi_C^2}}{T_C^{1/2}}$$

are quickly masked by the characteristics of the local proton distribution.

Figures 7 and 9 also illustrate the effect of selecting $r_{cs} = r_p$ in conjunction with the spherical plasmasphere model. Even after prolonged

exposure, $(1 + \phi)$ values are little altered. It is clear from these figures and Figures 3 and 4 that the decision concerning the most appropriate r_{cs} value to use in the creation collision term of Eqn. (10) is a minor one as regards the determination of the geocoronal kinetic distribution. This lack of sensitivity to r_{cs} carries over to macroscopic quantities: the two extreme values selected in this study yield practically identical results for the hydrogen atom density. In the remainder of this paper, the choice $r_{cs} = r_c$ is tacitly assumed.

Geocoronal Models

The evaporative model constructed using the new trajectory calculations is essentially the same as that described in GS1, even though an offset of 2° between the axes of computation is present. This indicates in itself that the Earth-Sun axis is not critical, in that quantities do not vary rapidly when moving away from axial position. The defining expressions for the quantities discussed in this section (density components, column density, kinetic temperature, and escape flux) are presented in GS1 (Eqns. (19)-(22)) where the summation schemes are also outlined. The discussion here is in terms of normalized quantities, with the normalization being in reference to the analytic $r_{cs} = r_c$ model, as this format highlights differences between the various models. The exobase parameters used in these calculations are given in Table 1.

Figure 10 shows the normalized hydrogen density profiles along the midnight axis for models incorporating either the spherical or the dipolar plasmasphere model, both with and without solar ionization, compared with the evaporative density profile. The models incorporating the dipolar plasmasphere model mimic the evaporative results closely, with an enhancement of densities

in the outer geocoronal region when solar ionization is ignored. The depletion of the exospheric content associated with the spherical plasmasphere model noted in GS1 is evident here, though the depletion is not as complete with the more rigorous formulation used here for the collision integrals. (Note that the calculations for the plasmasphere interaction have been extended down to the exobase.)

The majority of collisions in the dipolar plasmasphere interaction model occur within a few thousand kilometers of the exobase, producing higher energy bound atoms ($U^* < v_{esc}$) which in turn comprise the enhancement of density at higher altitudes. Although the loss term dominates at higher altitudes, it is too small to effectively alter the densities. In the spherical plasmasphere interaction model, while a net gain by faster trajectory parcels can occur near the exobase, the loss term does affect the density to comparatively high altitudes, resulting in the erosion shown in Figure 10. This line of argument indicates that while the spherical plasmasphere model should result in lower column densities compared to the evaporative values, the dipolar plasmasphere model should actually increase the column densities, in effect transferring near exobase atoms (which are quickly replenished) to higher altitudes with longer residence times. Column densities presented in Table 2 show that indeed this is the case.

Although solar ionization processes do not alter the character of the density profiles arising in the plasmasphere interaction models, the influence of solar ionization is not negligible at outer geocoronal locations. The satellite component at these altitudes (beyond geosynchronous radius) has limited exposure to the plasmasphere, most of which transpires away from the exobase where plasma temperatures are high so that destructive collisions dominate. These trajectories are not quasi-Keplerian orbits, but rather have

"perigees" that quickly rise away from the exobase. Hence, except near launch, the content of satellite trajectory parcels traversing the outer geocorona are effectively evaporative in nature and are noticeably eroded by solar ionization due to the long flight times involved. In contrast, at inner geocoronal locations (i.e., inside the plasmapause and especially within 2.00 R_E) the lower apogee ballistic and satellite atoms that comprise the bulk of the density are regulated by plasmaspheric charge exchange collisions; in these circumstances, solar ionization is not important due to the continual turnover of trajectory parcel content.

Figure 11 compares the geotail ratios (i.e., the ratio of the midnight axis densities to those along the noon axis) for the evaporative model and the dipolar plasmasphere interaction model both without and with solar ionization. In keeping with the generation of the geotail by radiation pressure dynamics, the geotail is little changed by the inclusion of a dipolar plasmasphere with or without solar ionization processes. The corresponding results for the spherical plasmasphere interaction models are not included, as these are essentially identical to the dipolar results. The dynamical underpinning of the geotail is blind to the manner by which trajectories are populated, and since local time variations of the topside ionosphere have been ignored, the geotail ratios computed here cannot exhibit differences between plasmasphere interaction models.

In Figure 12, the satellite fraction is shown for the same models referred to in Figure 10, along the midnight axis. As discussed above, considerable erosion of the satellite component with the too hot, too dense spherical plasmasphere is evident and the influence of solar ionization at outer geocoronal locations is also apparent. The dipolar plasmasphere model (without solar ionization) actually increases the satellite population at

outer geocoronal altitudes, reflecting the transfer of atoms near the exobase to higher energy bound orbits.

In Figure 13, kinetic temperatures for the evaporative (average of noon and midnight axis values) and the spherical and dipolar plasmasphere interaction models (midnight axis values) are shown along with the analytic $r_{cs} = r_p$ model temperatures. These are normalized with respect to the kinetic temperatures obtained with the analytic $r_{cs} = r_c$ model; again, the reason for preferring this manner of presentation is to emphasize the differences between various models and approaches in terms of a standard intelligible model. The resemblance of the evaporative and the dipolar plasmasphere interaction models to the analytic $r_{cs} = r_p$ model is again apparent. Solar ionization (not shown) acts to "warm" the outer geocoronal slightly (< 20 K) due to the preferential removal of slower atoms possessing longer flight times. (Regrettably, the kinetic temperatures computed for the analytic reference models of GS1 were incorrectly evaluated and do not have the proper asymptotic limits as $\lambda \to 0$. This mistake has been rectified in Figure 13.)

Lastly, in Figure 14, the escape flux arising with the spherical and dipolar plasmasphere models are shown, illustrating the well-known enhancement of hydrogen escape from the planet [Chamberlain, 1977; Maher and Tinsley, 1977]. The "albedo effect" correction described in Chamberlain [1977] has not been applied. Inclusion of the dipolar plasmasphere does not give as great an enhancement for the low-to-moderate solar activity parameter values used in this study. The "weakening" of the spherical plasmasphere interaction model escape flux at outer geocoronal radii was interpreted in GS1 as due to loss to hyperbolic flyby trajectories. A separate cause is responsible for the similar feature exhibited by the dipolar plasmasphere interaction model at radii beyond its plasmapause. Namely, escape trajectories originating at

polar locations and having little or no exposure to the dipolar plasmasphere begin making a contribution to the escape flux integral at radii greater than 4.00 R_E.

Characteristic Time Scales

The response time of the geocorona to changes in either exobase or plasmasphere conditions can be crudely estimated. For the simple evaporative case, solar photoionization indicates the average age shown in Figure 15, defined by

$$\langle T \rangle = T_{sol} \ln\left(\frac{N_{evap}}{N_{sol}}\right) \tag{16}$$

where N_{sol} is the density obtained when solar ionization is included without the plasmasphere interaction ($N^* = 0$) and T_{sol} is the solar ionization decay time. The "single pass" age is similarly defined, excluding the satellite contribution to the density. At inner geocoronal positions, the "single pass" age is the appropriate age to consider, not merely because orbiters do not comprise the major component but also because of the regulation of trajectory parcel content by plasmaspheric charge exchange collisions. At outer geocoronal locations, the "evaporative" age acts as an upper limit for a response time. These age estimates, defined in terms of net density and not the kinetic distribution function, might be useful in attempts to gauge the feedback of interactions of the exosphere with other components of geospace on the sources of exospheric hydrogen.

5. CONCLUDING REMARKS

The fundamental role played by radiation pressure dynamics in geocoronal structure has perhaps its most dramatic effect in establishing the geotail as a permanent feature. In light of this, it is appropriate to look upon "satellite" trajectories as being defined by the action of radiation pressure on atoms trapped in the planetary gravitational field, with the kinetic distribution along these trajectories then being determined by population mechanisms (e.g., exobase evaporation, charge exchange collisions with plasmaspheric protons, and solar ionization). In discussing the interaction with the plasmasphere, it is evident that the kinetic distribution function along a trajectory never attains to an equilibrium with the plasmaspheric proton distribution; this is due both to dynamical speed variations along exospheric trajectories and to spatial variations in plasmaspheric quantities. At radial distances of 2.00 R_E and beyond (within the plasmasphere), most collisions result in loss of bound component atoms via conversion to fast escaping atoms; in the dipolar plasmasphere interaction model evaluated here, though, such collisions are of minor significance because of the rapid decrease in proton densities away from the exobase. Collisions occurring near the exobase, on the other hand, can enhance the population of bound component satellite trajectories, even when the too hot, too dense spherical plasmasphere model is used (though in this case the enhancement only survives locally).

At the locations selected for evaluation in this work, the variation of plasma temperature with altitude is the most important revision to GS1 introduced by the dipolar plasmasphere model. The dipolar shape is not a major factor for points of evaluation along the Earth-Sun axis since this is a maximum exposure orientation of considerable symmetry; calculations with a

spherical plasmasphere model possessing the equatorial density and temperature profiles of the dipolar plasmasphere model introduced only slight variations to the dipolar plasmasphere interaction results shown in Figures 10-14. At other magnetic latitudes, and particularly at midlatitudes, features related to the dipolar shape would be more pronounced. The dipolar plasmasphere interaction model evaluated in this study is somewhat remarkable in not differing from the evaporative geocoronal model to any great extent. It is not likely that introducing "realistic" variations of steady state plasmaspheric parameters would alter this almost balanced situation to any great extent, at least for low-to-moderate solar conditions. This may indicate a considerable influence of the exosphere on plasmaspheric structure; an investigation of this point is certainly warranted. The comparative insensitivity of the plasmasphere interaction calculations to the zeroth-order density model in the creation integral of Eqn. (10) relates back to radiation pressure dynamics, in that satellite trajectories necessarily constitute a minor component in the velocity space at near-exobase locations irrespective of the mechanisms regulating the population of these trajectories. The assumption of no momentum exchange in the charge exchange reaction contributes to this insensitivity. The similarity of the GS1 spherical plasmasphere interaction results to those evaluated in this paper is a consequence of this, despite the differences in the treatment of the Boltzmann collision integral.

The advantage of the computational framework used here lies in the explicit nature of the trajectory selection and in the precision with which quantities can be evaluated at specified points. It also establishes a constructive framework for analysing and interpreting the results of Monte Carlo simulations. Hodges et al. [1981] and Tinsley et al. [1986] in particular report extensive studies using the Monte Carlo technique,

incorporating planetary rotation, exobase temperature nonuniformities, and thermospheric winds in addition to Lyman-α photon scattering and steady-state plasmasphere models; the more recent set of simulations [Tinsley, et al., 1986] explores geocoronal variations associated with the solar cycle and with the emptying of plasmaspheric content following magnetic substorms. These simulations demonstrate the importance of the plasma temperature profile on geocoronal kinetics and indeed the general modulation of exospheric content by the interaction with the plasmasphere. While the results of these simulations are useful in estimating exospheric parameters for a variety of applications, the physics involved is often not appreciated and some results have seemed puzzling. For example, it is difficult to gain any insight into the geotail phenomenon or into the characteristics of the outer geocoronal satellite population using Monte Carlo techniques, particularly when the subsequent analysis is couched in Keplerian terms. Also, some care must be exercised in assessing the meaning of the effective component "temperatures" presented by Tinsley et al. [1986, Figure 11]. In this regard, consider the analytic exosphere model with $r_{cs} = r_p$, possessing a complete bound component for $r < r_p$. For the exobase parameters used in this study, the analytic model kinetic temperature at an altitude of 750 km above the exobase remains near T_c (~1000K); the satellite component, taken alone, has an effective "temperature" of $T_{SAT} \approx 2850K$, reflecting the fast speeds of orbiting atoms near the exobase. This satellite "temperature" is given by [Chamberlain, 1963]

$$T_{SAT} = \frac{2}{3} T_c \langle \psi^2 \rangle_{SAT} = \frac{2T_c}{3}\left[\frac{\lambda^2}{\lambda_c + \lambda} + \frac{\gamma(\frac{5}{2}, x)}{\gamma(\frac{3}{2}, x)}\right]$$

where $\gamma(a,b)$ is the incomplete gamma function and $x = \lambda - \frac{\lambda^2}{\lambda_c + \lambda}$. At 2.00 R_E, where the satellite component comprises 1/5 of the total density, the

(complete) kinetic temperature drops to ~900K, yet $T_{SAT} \approx 1600K$ still exceeds T_c. The point is that the component contributions to the neutral kinetic temperature are largely determined by the gravitational potential, so that high transverse "temperatures" do not necessarily indicate a conversion to plasmaspheric temperatures. As regards the intuitive meaning of temperature, the exosphere cannot maintain plasmaspheric values, particularly at those radii where $U^* > v_{esc}$, because the neutral atoms are not "bottled" by the geomagnetic field. The solar cycle variations of the transverse "temperatures" reported in Tinsley et al. [1986] would seem rather to relate directly to the extent of the satellite component, in that in the solar minimum simulations this component was appreciably populated, making a significant contribution to the mean squared transverse velocity, while in the solar maximum simulations the satellite component was relatively eroded (refer to Figure 3 of Tinsley et al. [1986]) and the mean squared transverse velocity accordingly reduced. (Also note that the outward moving escape component "temperatures" presented in Figure 11 of Tinsley et al. [1986] are evidently not corrected for the non-zero effusion speeds associated with this component.) In brief, it is not plausible to look upon the geocorona as exhibiting a two-temperature structure with a transition to plasmasphere temperatures near 2.00 R_E.

The methodology employed throughout GS1 and this paper explicitly reveals the influence of solar radiation pressure, plasmaspheric charge exchange collisions, and solar ionization on geocoronal kinetics and structure, and is not limited to the simple cases so far studied. It can also be easily recast to permit calculation of quantities not discussed here. The accompanying paper on geocoronal line profiles [Bishop and Chamberlain, 1986] is an example of this.

ACKNOWLEDGMENTS

This research was sponsored by the National Aeronautics and Space Administration under grant NSG-7043, and by the Atmospheric Research Section, National Science Foundation, under grant ATM-8415118, both to Rice University.

REFERENCES

Bertaux, J. L., and J. E. Blamont, Interpretation of OGO 5 Lyman alpha measurements in the upper geocorona, J. Geophys. Res., 78, 80-91, 1973.

Bishop, J., Geocoronal structure: The effects of solar radiation pressure and the plasmasphere interaction, J. Geophys. Res., 90, 5235-5245, 1985.

Bishop, J., and J. W. Chamberlain, Geocoronal Structure 3: Optically thin, Doppler broadened line profiles, submitted to J. Geophys. Res., 1986.

Chamberlain, J. W., Planetary coronae and atmospheric evaporation, Planet Space Sci., 11, 901-960, 1963.

Chamberlain, J. W., Charge exchange in a planetary corona: Its effect on the distribution and escape of hydrogen, J. Geophys. Res., 82, 1-9, 1977.

Chamberlain, J. W., Depletion of satellite atoms in a collisionless exosphere by radiation pressure, Icarus, 39, 286-294, 1979.

Chiu, Y. T., J. G. Luhmann, B. K. Ching, and D. J. Boucher, Jr., An equilibrium model of plasmaspheric composition and density, J. Geophys. Res., 84, 909-916, 1979.

Fahr, H. J., and B. Shizgal, Modern exospheric theories and their observational relevance, Rev. Geophys. Space Phys., 21, 75-124, 1983.

Hodges, R. R., R. P. Rohrbaugh, and B. A. Tinsley, The effect of the charge exchange source on the velocity and "temperature" distributions and their anisotropies in the Earth's exosphere, J. Geophys. Res., 86, 6917-6925, 1981.

Li, W., J. J. Sojka, and W. J. Raitt, A study of plasmaspheric density distributions for diffusive equilibrium conditions, Planet. Space Sci., 31, 1315-1327, 1983.

Maher, L. J., and B. A. Tinsley, Atomic hydrogen escape rate due to charge exchange with hot plasmaspheric ions, J. Geophys. Res., 82, 689-695, 1977.

Tinsley, B. A., R. R. Hodges, Jr., and R. P. Rohrbaugh, Monte-Carlo models for the terrestrial exosphere over a solar cycle, J. Geophys. Res., manuscript submitted, 1986.

Thomas, G. E., and R. C. Bohlin, Lyman-alpha measurements of neutral hydrogen in the outer geocorona and in interplanetary space, J. Geophys. Res., 77, 2752-2761, 1972.

Wallace, L., C. A. Barth, J. B. Pearce, K. K. Kelly, D. E. Anderson, Jr., and W. G. Fastie, Mariner 5 measurement of the Earth's Lyman alpha emission, J. Geophys. Res., 75, 3769-3777, 1970.

FIGURE CAPTIONS

Fig. 1. Comparison of the evaporative geotail density ratio with the ratio of velocity space volume elements Δ_v for the bound component.

Fig. 2. Kinetic distributions at 2.00 R_E for motion along the Earth-Sun axis on the dayside ($\chi = 0°$), computed using the spherical plasmasphere (curve S) and dipolar plasmasphere (curve D) models, both with $r_{cs} = r_c$ in the creation collision integral of Eqn. (10). The evaporative distribution is also shown (curve RP) and has been used for normalization.

Fig. 3. Enhancement factors for the bound components of the kinetic distributions shown in Figure 2 (curves D and $S(r_c)$). Also shown are values computed with solar ionization augmenting the dipolar plasmasphere interaction (curve D+SI) and by evaluating the spherical plasmasphere interaction with $r_{cs} = r_p$ in Eqn. (10) (curve $S(r_p)$). The speed needed to pierce the spherical plasmapause at this altitude is $\psi = 1.6$.

Fig. 4. Enhancement factors for motion transverse to the $\chi = 0°$ axis at 2.00 R_E, showing the effect of the spherical plasmasphere for two choices of r_{cs} in evaluating Eqn. (10) (curves $S(r_c)$ and $S(r_p)$). Two orientations of the dynamical plane with respect to the magnetic equator have been chosen in conjunction with the dipolar plasmasphere model (curves D,0° and D,90°, evaluated with $r_{cs} = r_c$ in Eqn. (10)). Also shown is the dipolar plasmasphere enhancement factor

incorporating solar ionization and averaged over all dynamical plane orientations (curve D_{AVE}+SI).

Fig. 5. Variation of the enhancement factor in the dipolar (D) and spherical ($S(r_c)$ and $S(r_p)$, indicating the r_{cs} value assumed in Eqn. (10)) plasmasphere interaction models along a ballistic trajectory coincident with the $\chi = 0°$ axis, as a function of time of flight between launch from and return to the exobase ($\psi_c = 2.211$) . Apogee and 2.00 R_E occasions are indicated along the axis of abscissas.

Fig. 6. Variation of the enhancement factor for the models considered in Figure 5 along an escaping trajectory ($\mu = {}^{+}1$) coincident with the noon ($\chi = 0°$) axis, as a function of time of flight above the exobase ($\psi_c = 3.448$). Capture counterparts ($\mu = {}^{-}1$) are also shown. Intersection with the plasmapause locations, along with 2.00 R_E occasion, are indicated along the axis of abscissas.

Fig. 7. Variation of the enhancement factor along selected orbits of a trajectory that exhibits 32 1/2 loops about the planet (launched near morning terminator, prograde motion, with $\chi_c = -0.562\pi$, $\psi_c = 2.203$, and $\delta_c = 0.466\pi$) Two orientations of the dynamical plane with respect to the magnetic equator are illustrated in conjunction with the dipolar plasmasphere. The spherical plasmasphere enhancement factors have been evaluated using the indicated r_{cs} values in Eqn. (10). Occasions of apogee and perigee for each orbit are indicated.

Fig. 8. Relative magnitude variations of the production (P) and loss (L) terms of Eqn. (10) along the orbits of Figure 7, for the D,0° and $S(r_c)$ cases. (The subscripts on the ordinate axis label are meant to indicate that P and L are separately displayed, not that one or the other has been held constant.)

Fig. 9. Evolution of the enhancement factor at the time of evening terminator crossing, for the trajectory and cases considered in Figure 7.

Fig. 10. Normalized density profiles along the midnight (χ = 180°) axis, for the dipolar (D) and spherical (S) plasmasphere interaction models, both without and with solar ionization (SI). The evaporative midnight density profile is also shown (RP). Normalization is with respect to the analytic $r_{cs} = r_c$ model.

Fig. 11. Geotail density ratios for the dipolar plasmasphere interaction model (D), without and with solar ionization (SI). The evaporative geotail profile is also shown (RP). Geotail ratios arising in the spherical plasmasphere interaction are effectively indistinguishable from the corresponding D, D+SI ratios.

Fig. 12. Satellite fractional density profiles along the midnight axis for the cases shown in Figure 10. Satellite fractions along the noon (χ = 0°) axis are smaller than the corresponding midnight values at outer geocoronal locations and exhibit similar profile shapes (~30% smaller at the outermost evaluation point in the spherical

plasmasphere interaction models, ~20% smaller in the dipolar plasmasphere interaction and evaporative models).

Fig. 13. Normalized kinetic temperature profiles for the dipolar (D) and spherical (S) plasmasphere interaction models, along the midnight axis. Also shown are the normalized temperatures for the evaporative model (RP, average of noon and midnight axis values) and the analytic $r_{cs} = r_p$ model. Normalization is with respect to the analytic $r_{cs} = r_c$ model.

Fig. 14. Normalized escape flux profiles for the dipolar (D) and spherical (S) plasmasphere interaction models, along both noon and midnight axes. Also shown are the evaporative model (RP) noon and midnight profiles. Normalization is with respect to the analytic $r_{cs} = r_c$ model (i.e., the Jeans escape flux).

Fig. 15. Effective ages of exospheric hydrogen, as defined in Eqn. (16), computed using all evaporatively generated components and using only ballistic + escaping ("single pass") components.

TABLE 1. Geocoronal and Plasmasphere Parameters

PLASMASPHERE MODELS

	Temperature (K)	Exobase Density (cm^{-3})	Plasmapause Location
Spherical:			
	4080	10^4 (H^+)	$r_{pp} = 6.632\ R_E$
Dipolar*:			
	2000-5000 T_o = 2000K ΔT = 3000K $\beta = \gamma = 1/2$ $L_o = 3.00\ R_E$	4.00×10^3 (H^+) 2.00×10^5 (O^+) 2.04×10^5 (e^-)	$L_{pp} = 4.00\ R_E$

EXOBASE PARAMETERS: $T_c = 1020K$, $N_c = 8.0 \times 10^4\ cm^{-3}$

RADIATION PRESSURE ACCELERATION: $a = 0.75\ cm/sec^2$ ($r_p = 36.20\ R_E$)

SOLAR IONIZATION DECAY TIME: $T_{sol} = 10$ days

*Refer to Eqn. (11) for the temperature profile used in this model.

TABLE 2. Column Densities Above Exobase

Model	N_{col} (10^{13} atoms/cm^2)
EVAPORATIVE	
Noon ($\chi = 0°$)	1.217 (1.183)
Midnight ($\chi = 180°$)	1.236 (1.200)
SPHERICAL PLASMASPHERE	
Noon	1.116 (1.108)
Midnight	1.133 (1.123)
DIPOLAR PLASMASPHERE	
Noon	1.235 (1.202)
Midnight	1.253 (1.220)

NOTE: Quantities in parentheses refer to models incorporating solar ionization via Eqn. (15). A ceiling has been placed at the exopause. Refer to GS1, Eqn. (22).

FIG. 1

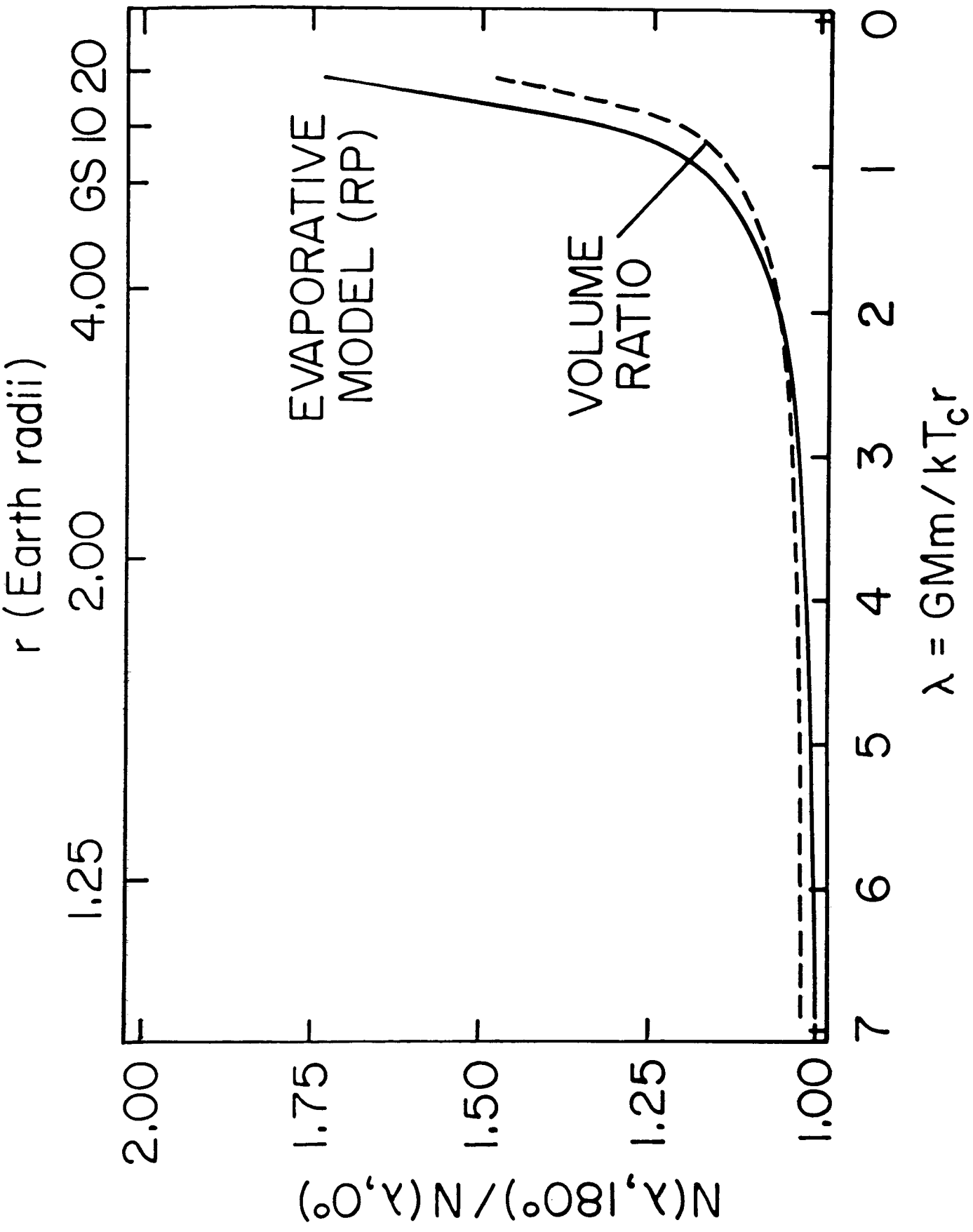
r (Earth radii)
1.25
2.00
4.00
GS
10
20
EVAPORATIVE MODEL (RP)
VOLUME RATIO
2.00
1.75
1.50
1.25
1.00
N(λ, 180°) / N(λ, 0°)
0
1
2
3
4
5
6
7
λ = GMm / kT_c r

FIG. 2

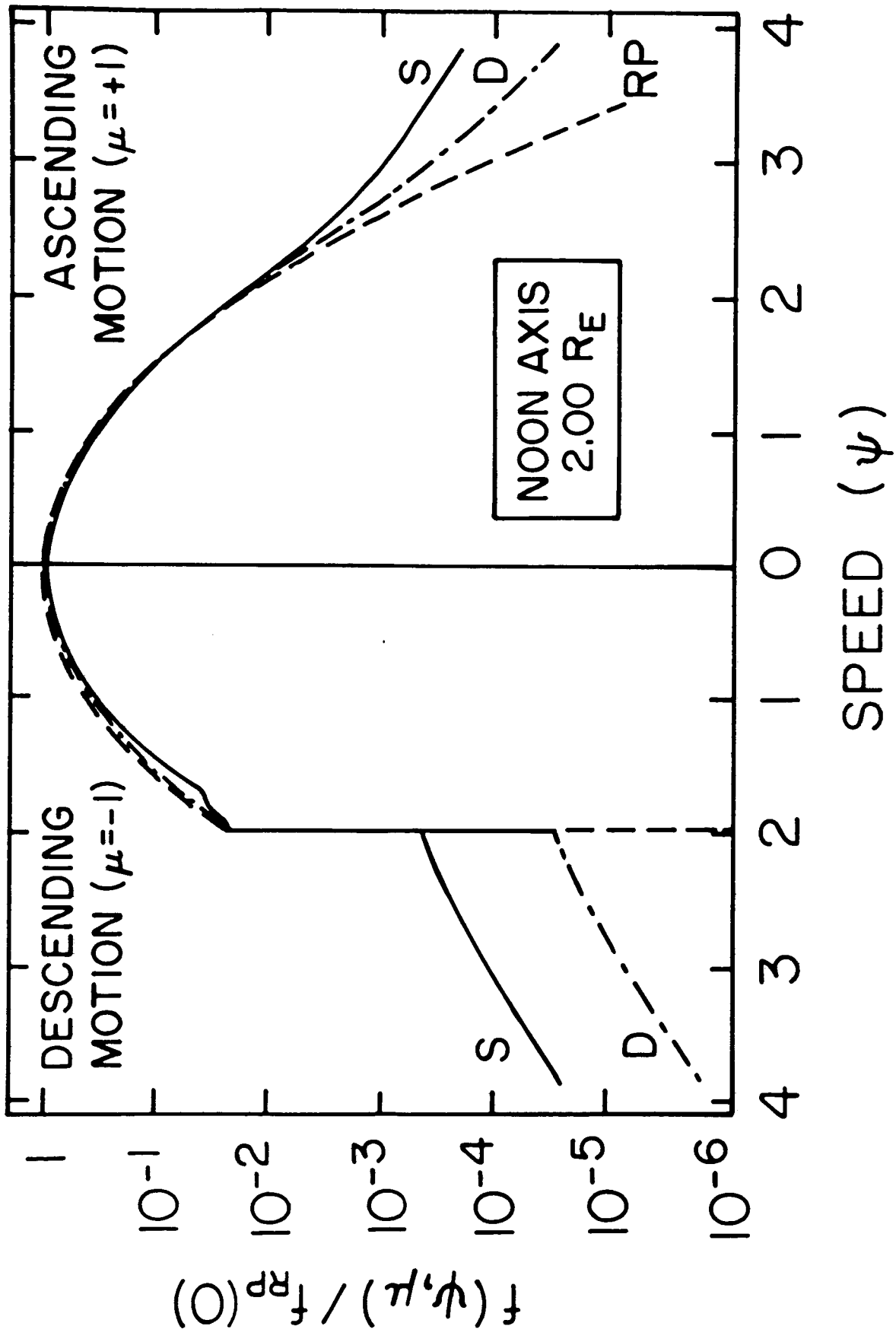
ASCENDING
MOTION (μ=+1)
DESCENDING
MOTION (μ=-1)
S
D
RP
NOON AXIS
2.00 R_E
SPEED (ψ)
f(ψ,μ) / f_RP(0)
1
10^-1
10^-2
10^-3
10^-4
10^-5
10^-6
0
1
2
3
4

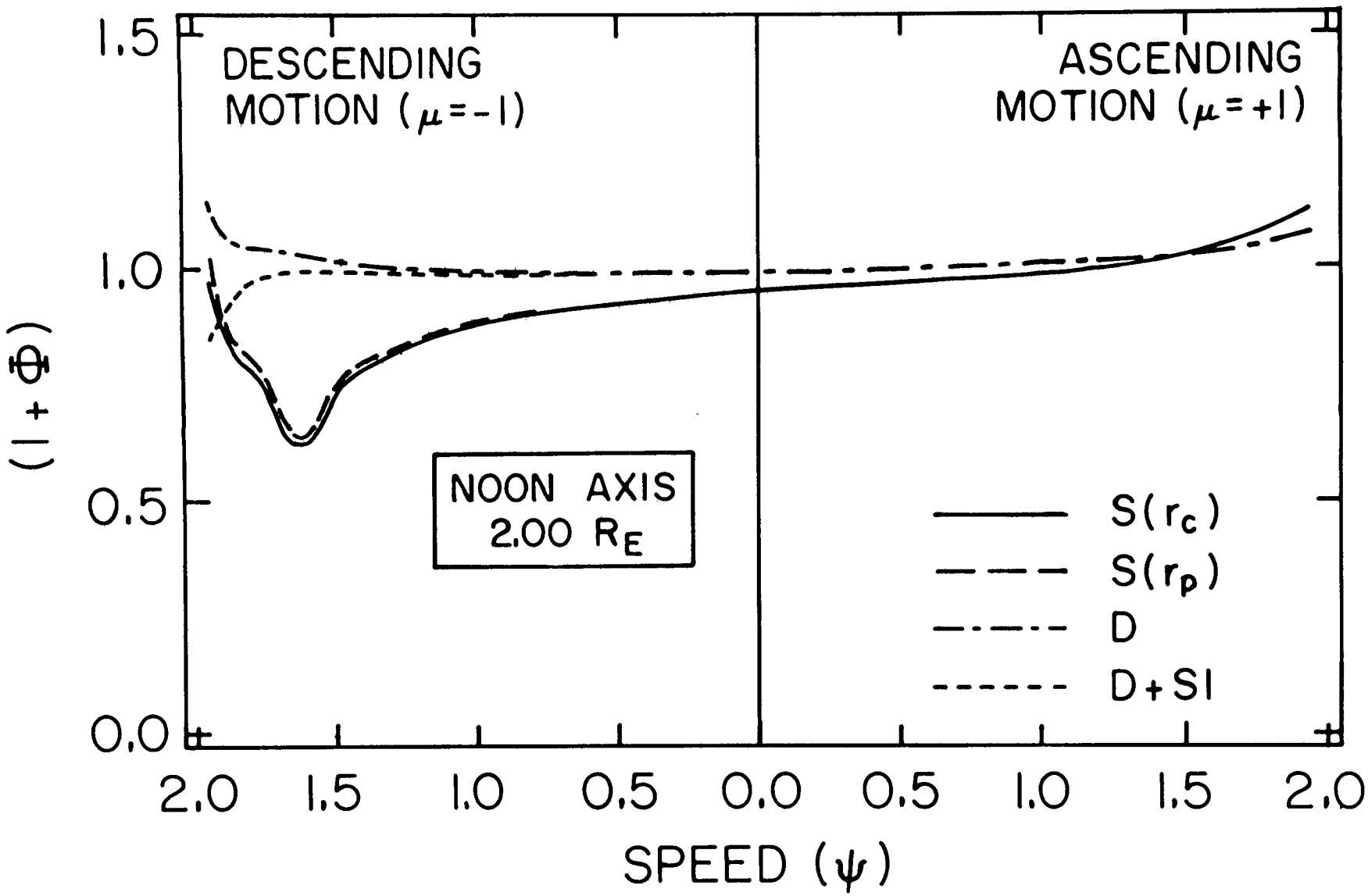
DESCENDING
MOTION (μ=-1)
ASCENDING
MOTION (μ=+1)
NOON AXIS
2.00 R_E
S(r_c)
S(r_p)
D
D+SI
1.5
1.0
0.5
0.0
2.0
1.5
1.0
0.5
0.0
0.5
1.0
1.5
2.0
SPEED (ψ)
($1+\Theta$)

FIG. 3

FIG. 4

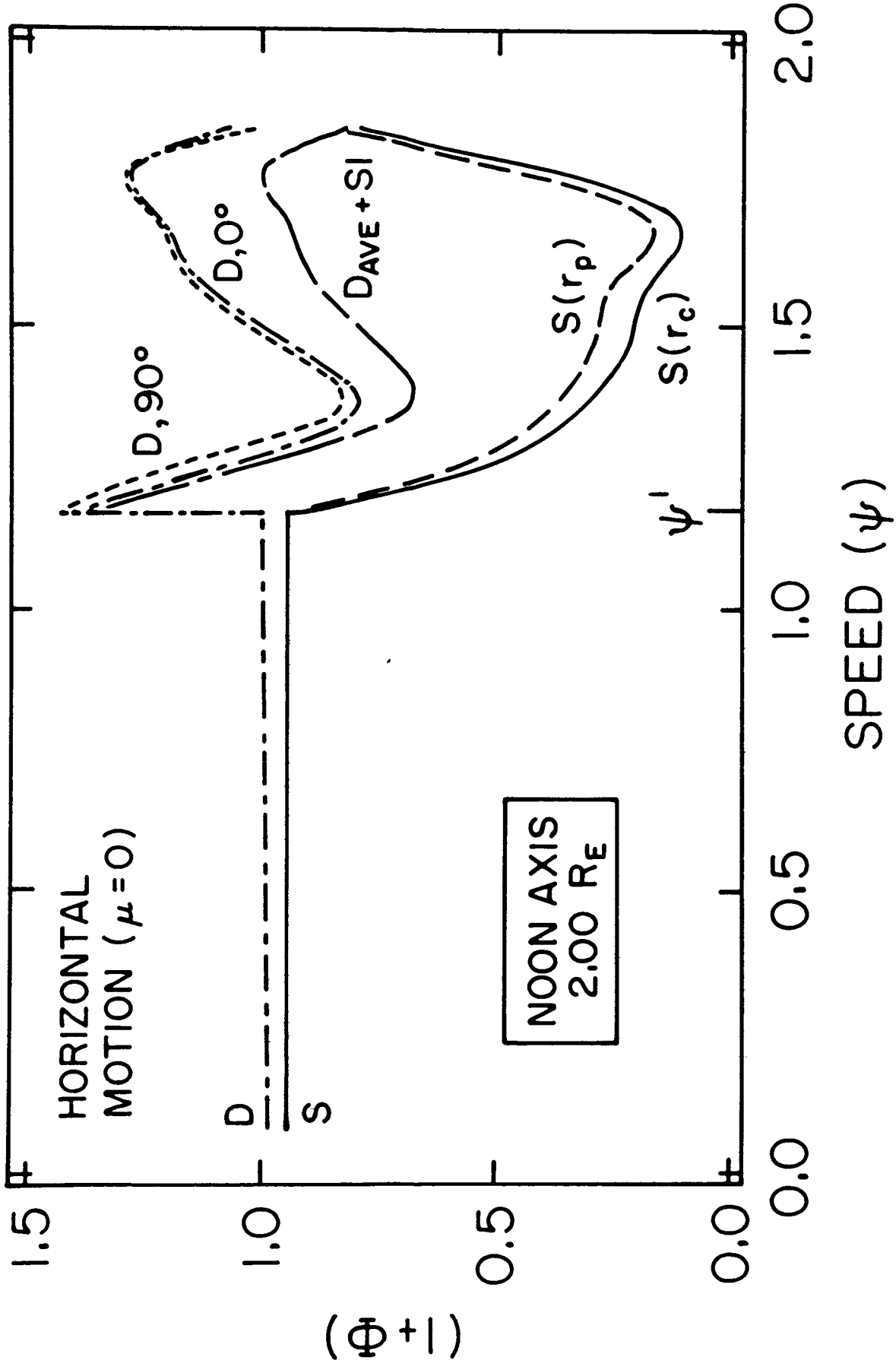
(1+Φ)
1.5
1.0
0.5
0.0
0.0
0.5
1.0
1.5
2.0
SPEED (ψ)
ψ'
HORIZONTAL MOTION (μ=0)
D
S
D,90°
D,0°
D_AVE+SI
S(r_p)
S(r_c)
NOON AXIS
2.00 R_E

FIG. 5

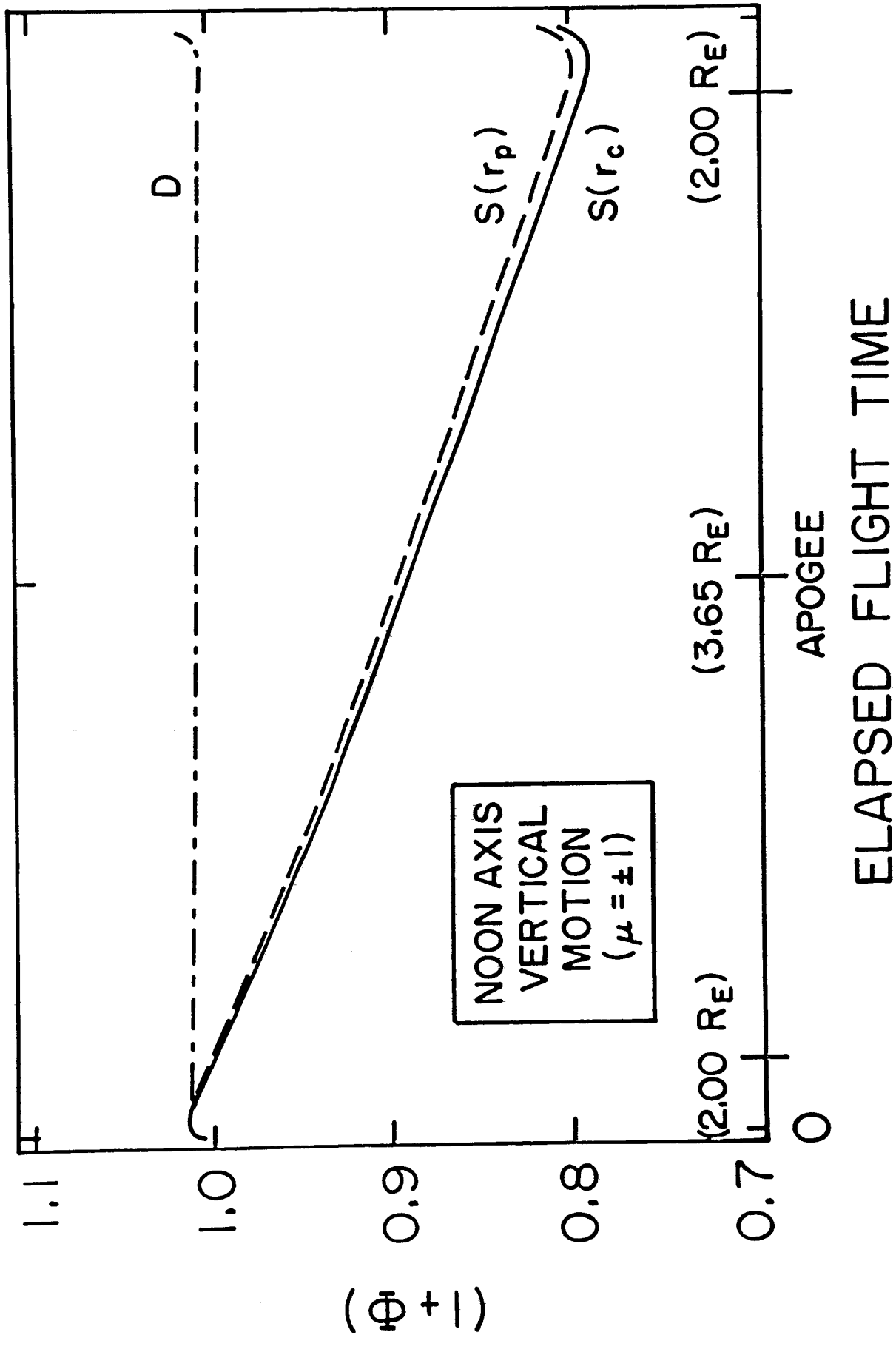
(Φ + 1)
1.1
1.0
0.9
0.8
0.7
D
S(r_p)
S(r_c)
NOON AXIS
VERTICAL
MOTION
(μ = ±1)
(2.00 R_E)
(3.65 R_E)
(2.00 R_E)
0
APOGEE
ELAPSED FLIGHT TIME

FIG. 6

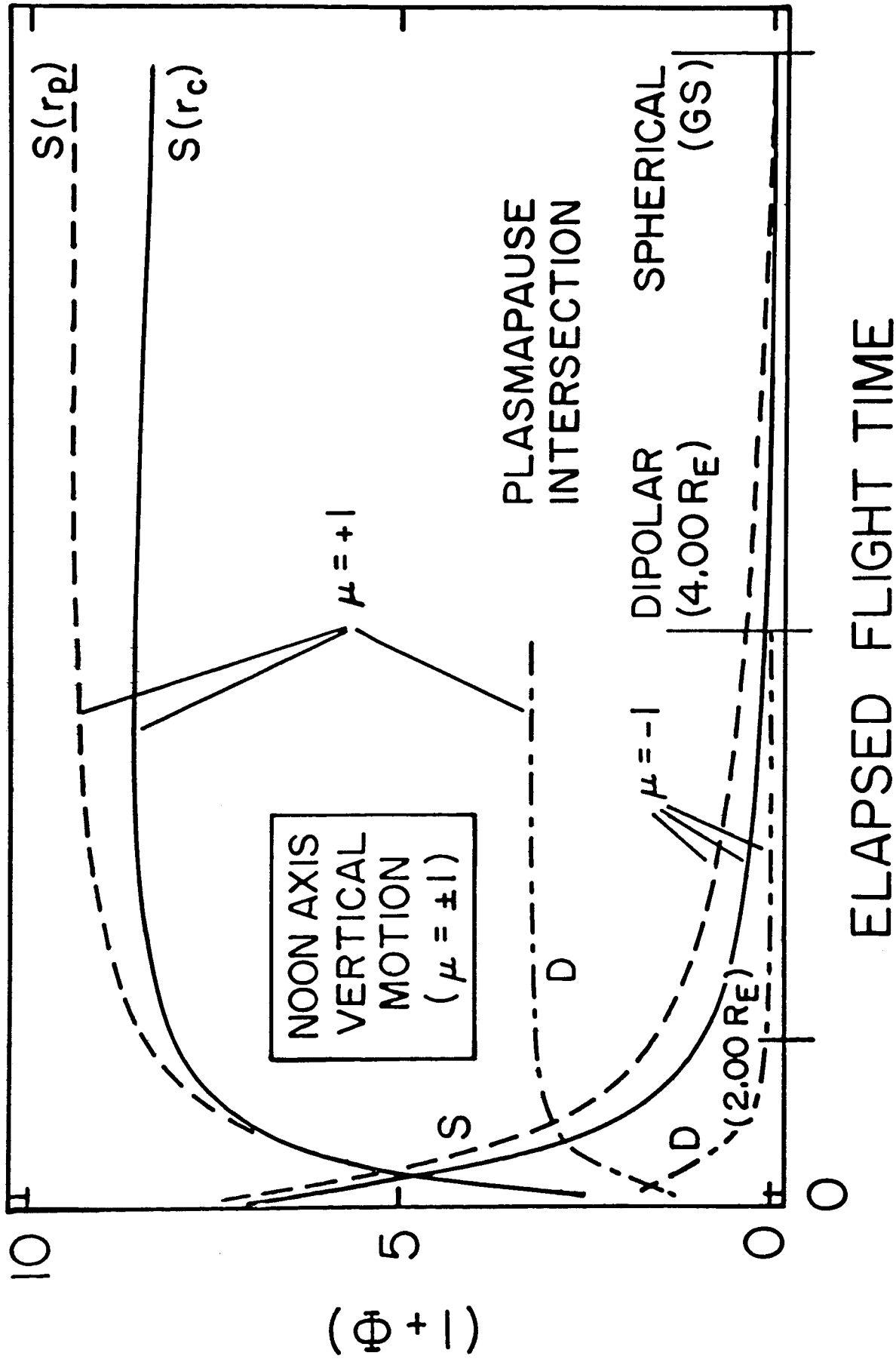
S(rp)
S(rc)
PLASMAPAUSE INTERSECTION
SPHERICAL (GS)
DIPOLAR (4.00 RE)
μ = +1
μ = -1
NOON AXIS VERTICAL MOTION (μ = ±1)
D
S
D
(2.00 RE)
10
5
0
0
(Φ + 1)
ELAPSED FLIGHT TIME

FIG. 7

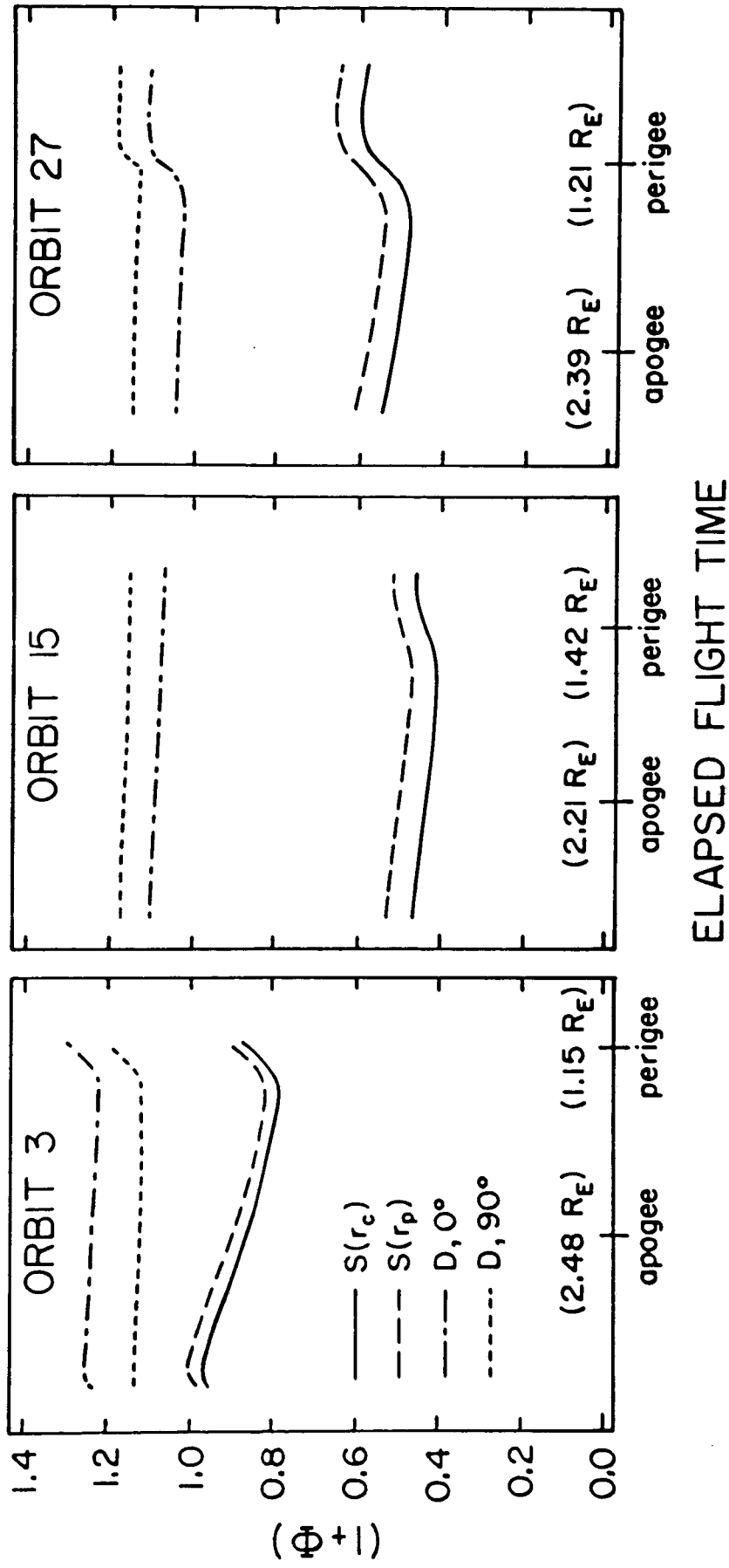
ORBIT 3
ORBIT 15
ORBIT 27
S(r_c)
S(r_p)
D, 0°
D, 90°
(2.48 R_E)
(1.15 R_E)
(2.21 R_E)
(1.42 R_E)
(2.39 R_E)
(1.21 R_E)
apogee
perigee
1.4
1.2
1.0
0.8
0.6
0.4
0.2
0.0
(Φ + 1)
ELAPSED FLIGHT TIME

FIG. 8

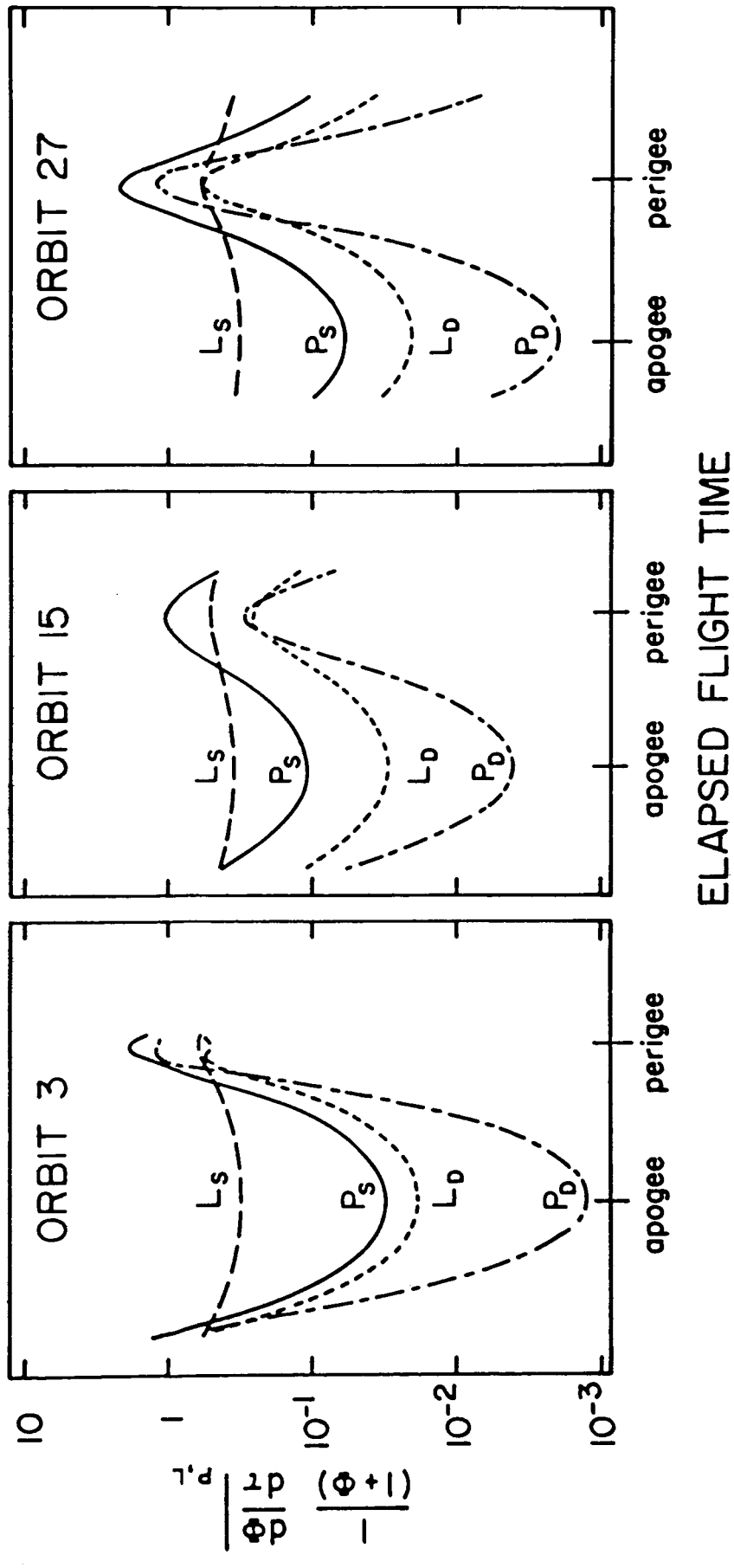
ORBIT 3
ORBIT 15
ORBIT 27
L_S
P_S
L_D
P_D
apogee
perigee
ELAPSED FLIGHT TIME
$\frac{1}{(1+\Phi)} \left| \frac{d\Phi}{d\tau} \right|_{P,L}$
10
1
10^{-1}
10^{-2}
10^{-3}

FIG. 9

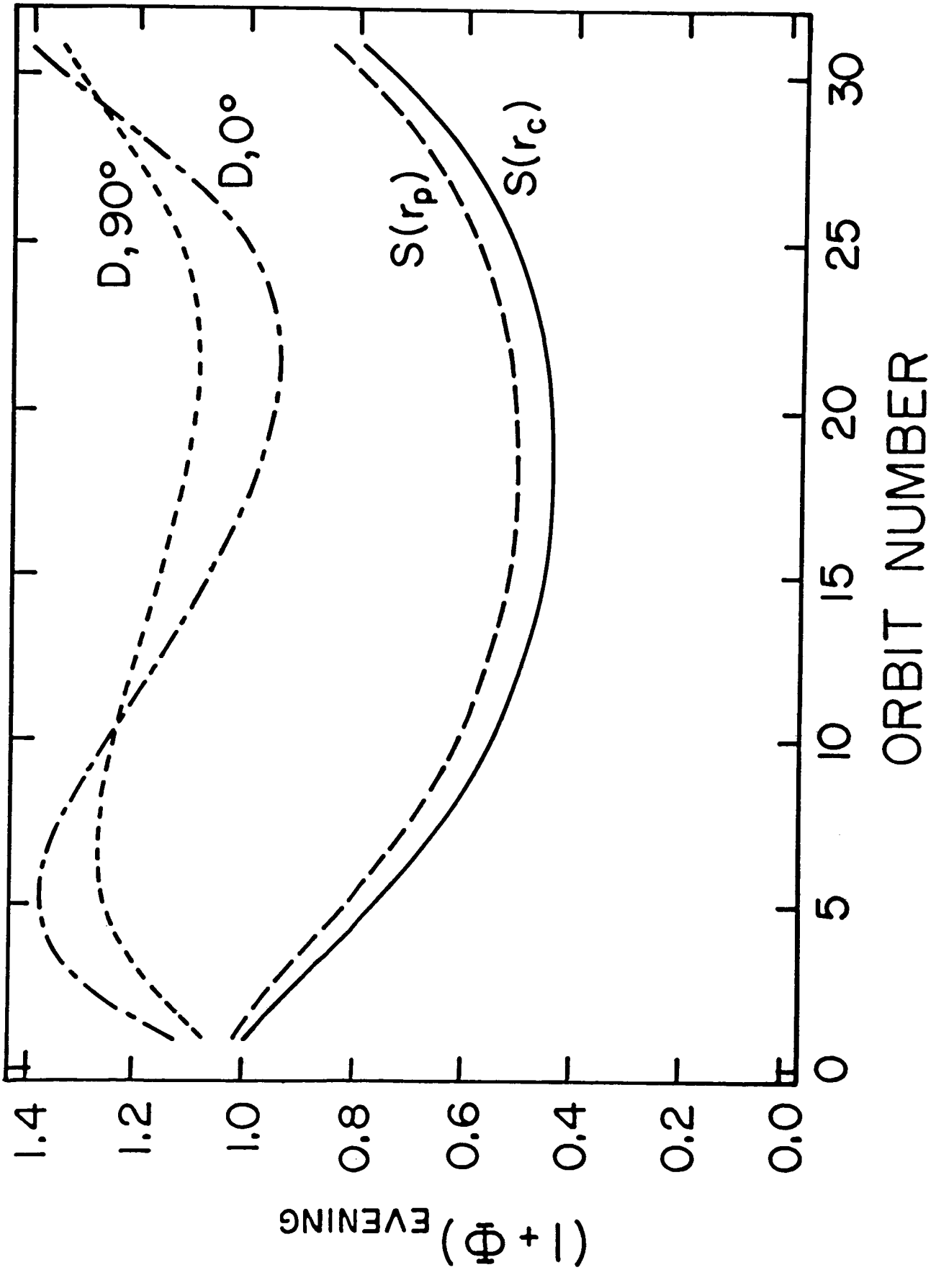
D,90°
D,0°
S(r_p)
S(r_c)
ORBIT NUMBER
0
5
10
15
20
25
30
1.4
1.2
1.0
0.8
0.6
0.4
0.2
0.0
(1 + Φ) EVENING

FIG. 10

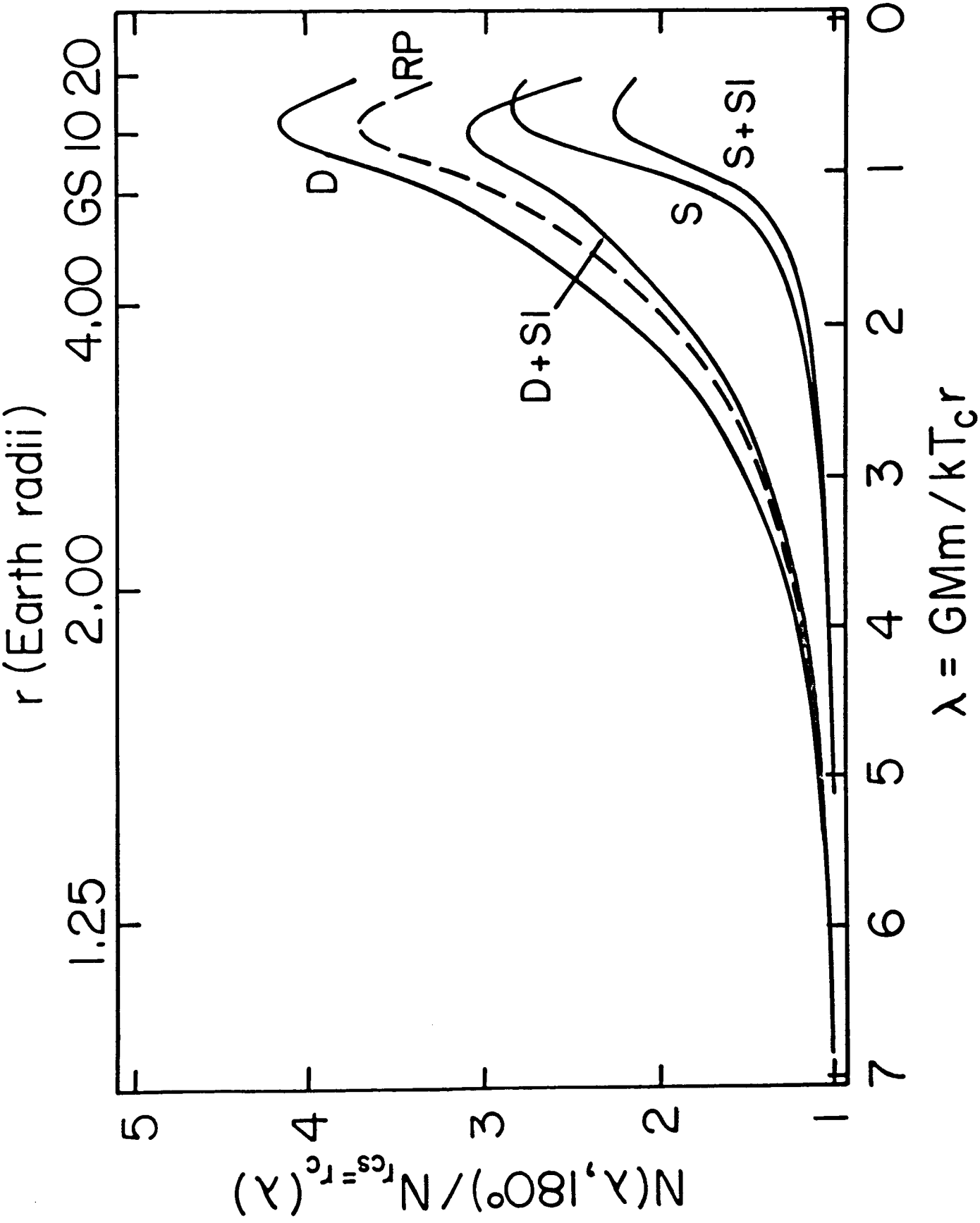
r (Earth radii)
1.25
2.00
4.00 GS 10 20
D
RP
D+SI
S
S+SI
$N(\lambda, 180°)/N_{r_{cs}=r_c}(\lambda)$
$\lambda = GMm/kT_c r$

FIG. 11

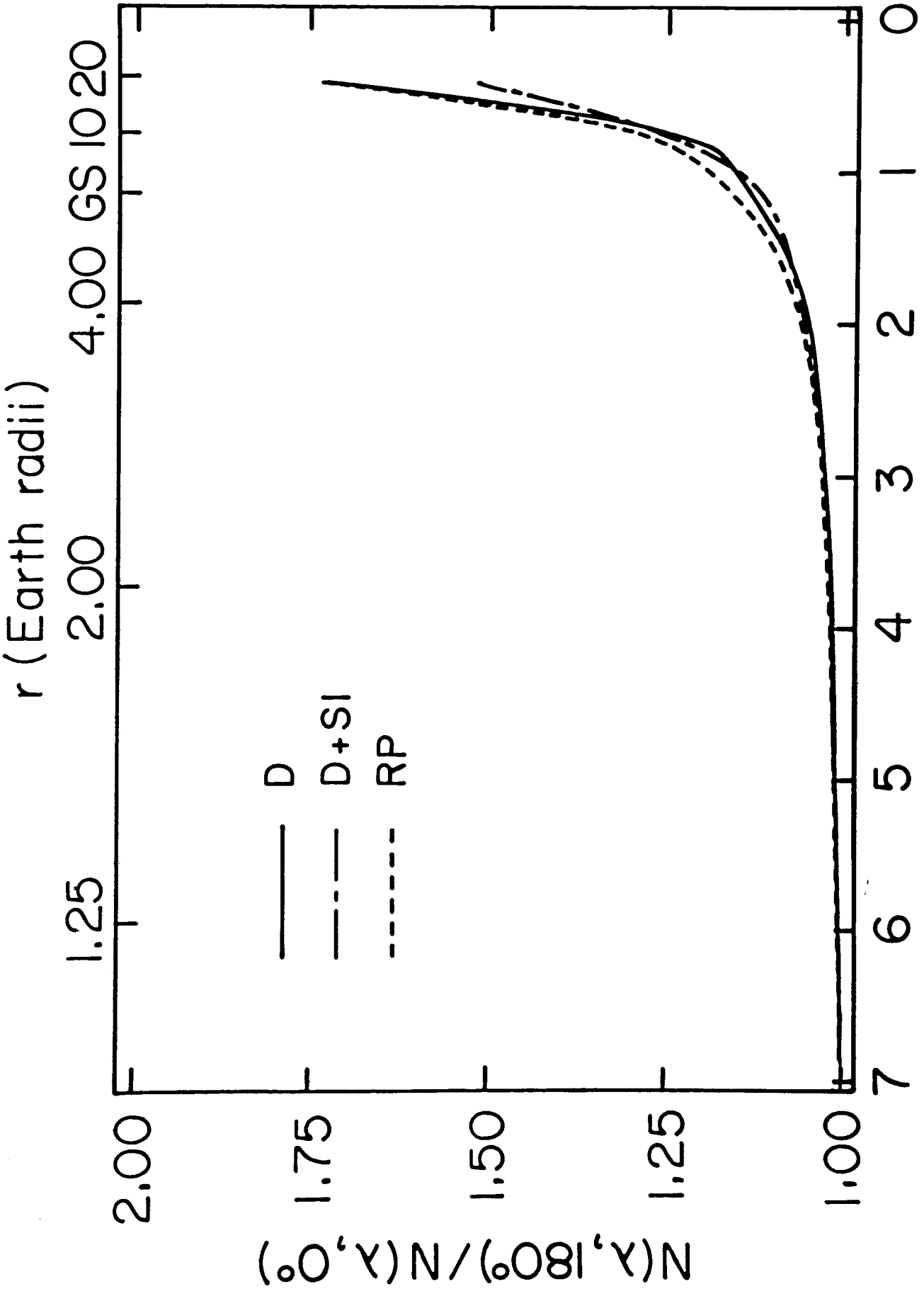
r (Earth radii)
4.00 GS 1020
2.00
1.25
D
D+SI
RP
λ = GMm/kT_cr
0
1
2
3
4
5
6
7
2.00
1.75
1.50
1.25
1.00
N(λ,180°)/N(λ,0°)

FIG. 12

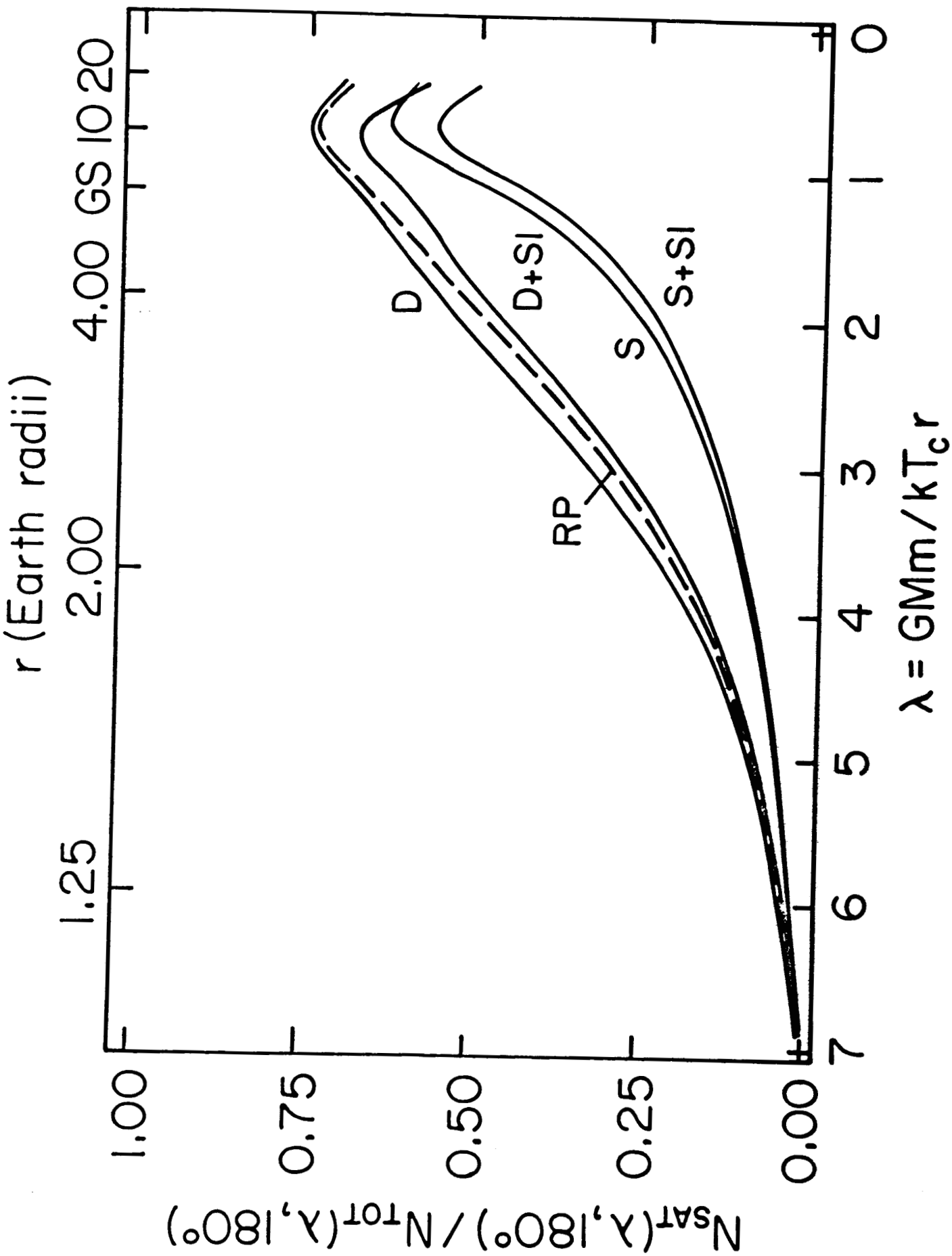
r (Earth radii)
1.25
2.00
4.00 GS 10 20
1.00
0.75
0.50
0.25
0.00
$N_{sat}(\lambda,180°)/N_{tot}(\lambda,180°)$
0
1
2
3
4
5
6
7
$\lambda = GMm/kT_c r$
D
D+SI
S
S+SI
RP

FIG. 13

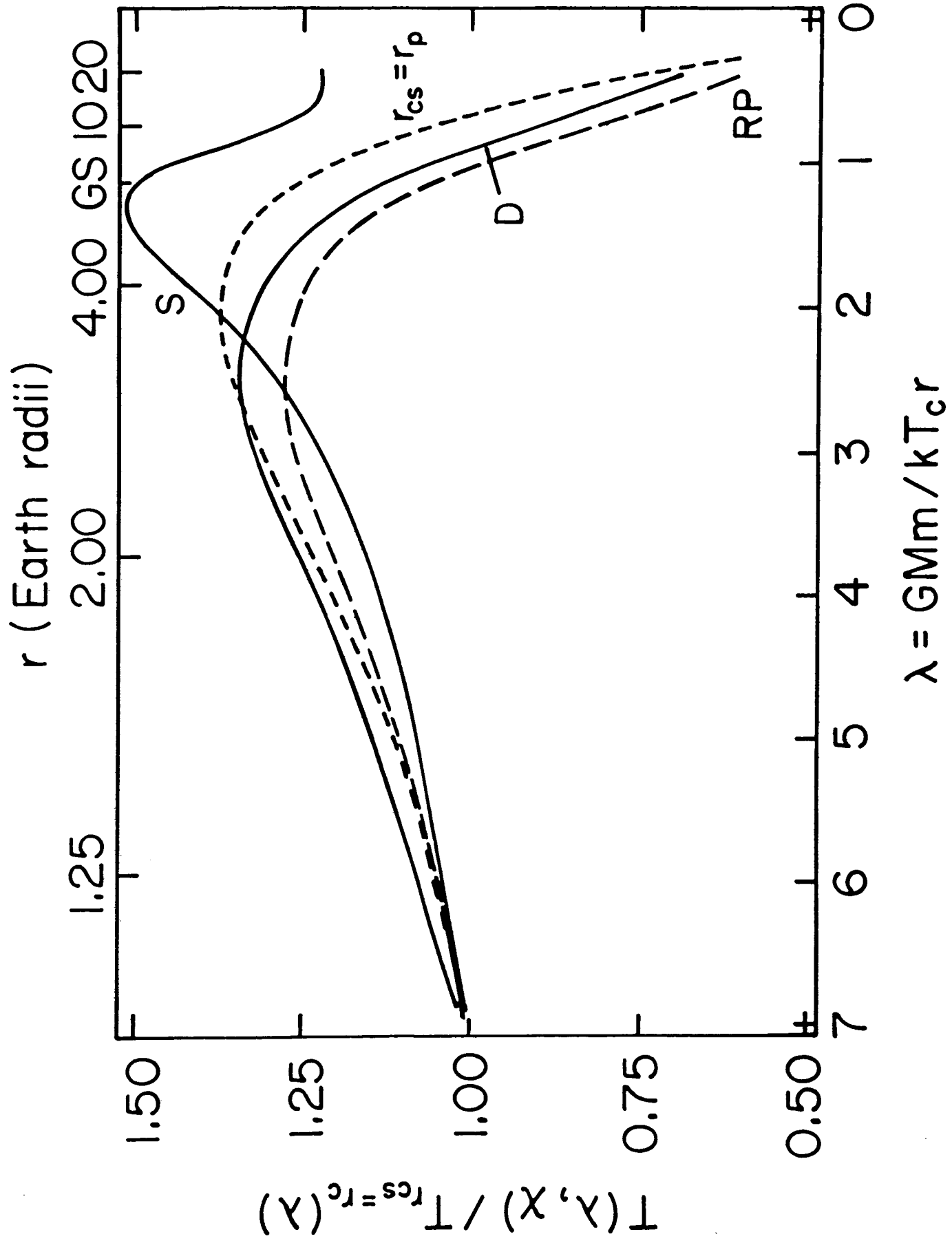
r (Earth radii)
4.00 GS 1020
2.00
1.25
S
$r_{cs} = r_p$
D
RP
$\lambda = GMm/kT_c r$
$T(\lambda, \chi) / T_{r_{cs}=r_c}(\lambda)$
1.50
1.25
1.00
0.75
0.50
0
1
2
3
4
5
6
7

FIG. 14

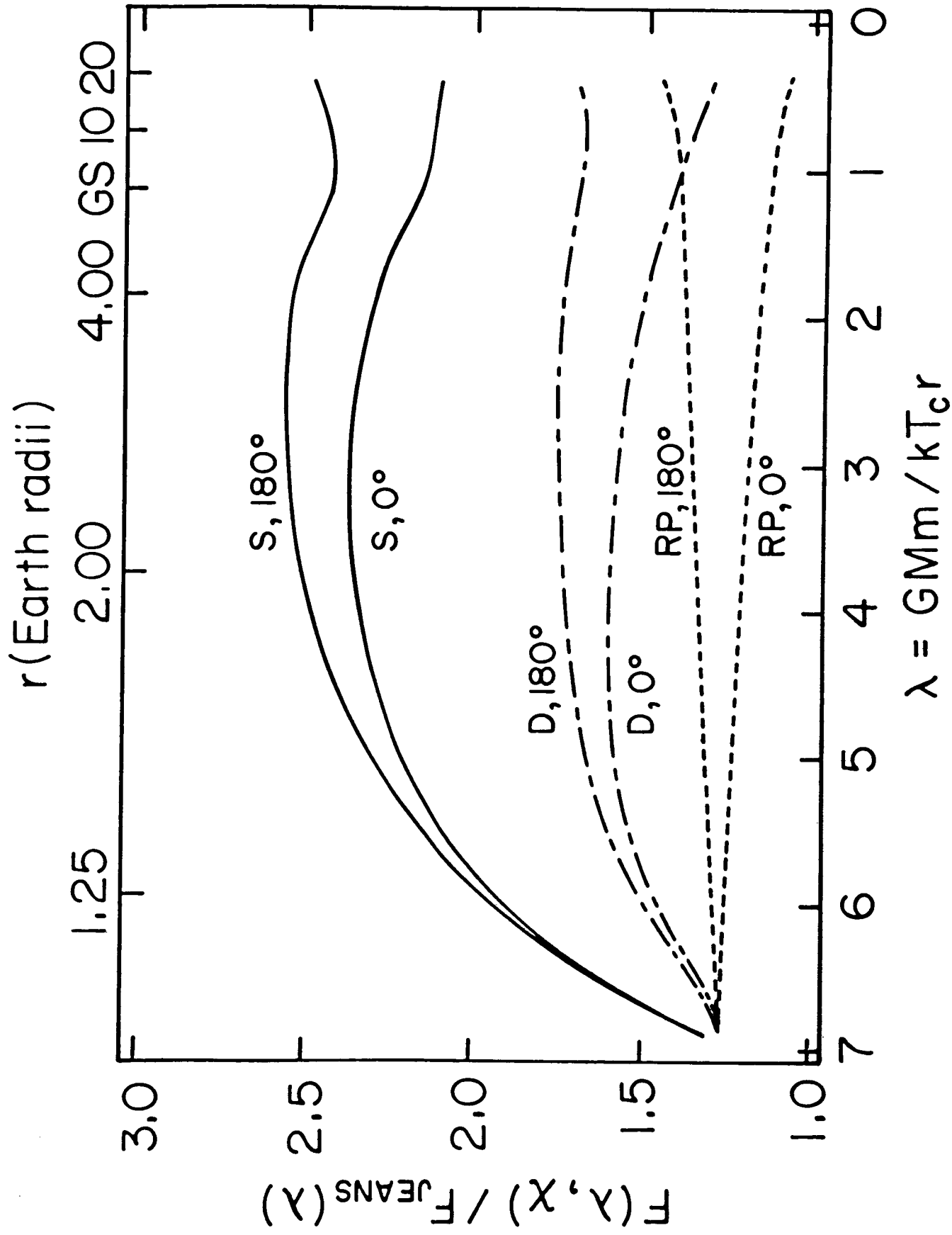
r(Earth radii)
1.25
2.00
4.00
GS 10 20
S, 180°
S, 0°
D, 180°
D, 0°
RP, 180°
RP, 0°
3.0
2.5
2.0
1.5
1.0
0
1
2
3
4
5
6
7
λ = GMm / kT_c r
F(λ, χ) / F_JEANS(λ)

FIG. 15

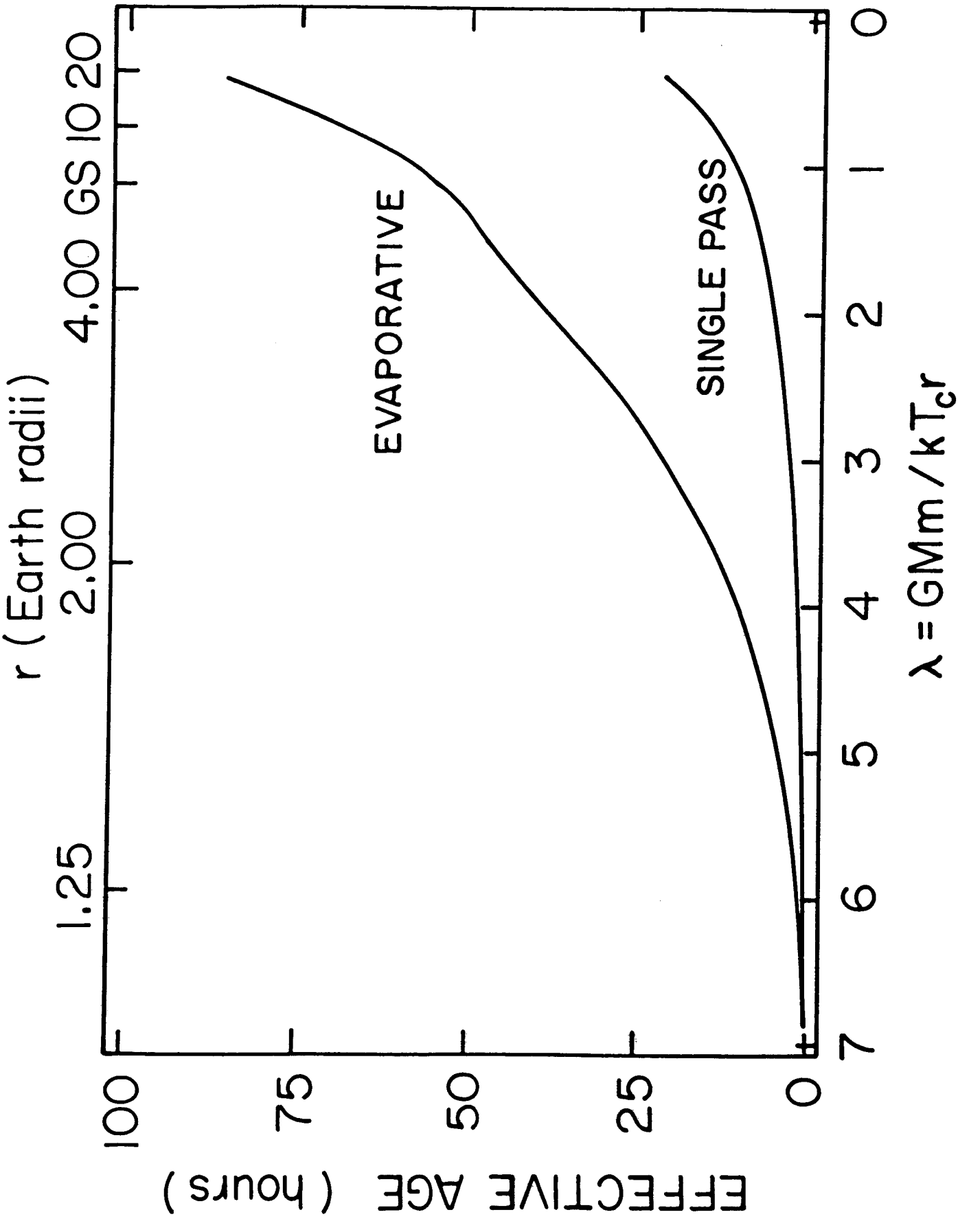
EFFECTIVE AGE (hours)
100
75
50
25
0
r (Earth radii)
1.25
2.00
4.00 GS 10 20
EVAPORATIVE
SINGLE PASS
0
1
2
3
4
5
6
7
λ = GMm / kT_c r